

New Materials for Thermal Barrier Coatings



Feifei Zhou and Shun Wang

Abstract Thermal barrier coatings (TBCs) are essential for protecting hot-end components of aero-engine and gas turbine against thermal and corrosion damage, thereby improving thermal efficiency and extending its service life. The selection of TBCs materials is crucial including high melting point, low thermal conductivity, corrosion resistance, thermal expansion coefficient, substrate matching, and no phase transformation or sintering during service. Yttrium-stabilized zirconia (YSZ) is a typical material with desirable properties, but it cannot withstand temperatures above 1200 °C for prolonged service. Novel TBCs materials have been developed, including rare earth zirconate, hexaluminate, niobates, and tantalates. This chapter presents an overview of oxide TBCs materials, focusing on rare earth zirconate TBCs and the influence of ion doping, as well as the crystal structures and thermodynamic properties of niobates and tantalates. Finally, this summary work provides insight into the development of TBCs materials.

Keywords Thermal barrier coatings · Novel materials · Rare earth doping

1 Metal Oxide and Their Doped Materials

Among the metal oxides, zirconia (ZrO_2)-based materials are the most widely used in thermal barrier coatings. In order to improve the performance of ZrO_2 -based coatings, doping modification is usually carried out on materials, among which rare

F. Zhou (✉)

School of Materials Science and Engineering, Harbin Institute of Technology, Harbin 150001, People's Republic of China
e-mail: snowy_hit@163.com

Zhengzhou Research Institute, Harbin Institute of Technology, Zhengzhou 450000, People's Republic of China

S. Wang

Institute of Advanced Structure Technology, Beijing Institute of Technology, Beijing, People's Republic of China

earth oxides are widely used in the modification of thermal barrier coatings. This section introduces ZrO_2 -based materials as the main object.

1.1 Crystal Structure and Thermal Properties of Materials

Zirconia (ZrO_2) is an excellent functional and structural integration material [1–5] which is highly abundant and inexpensive. As a high-temperature structural ceramic material, ZrO_2 has the reputation of “ceramic steel” and has been widely used in many industrial fields in recent years. ZrO_2 exhibits high melting point, strength, hardness, toughness, friction resistance, low thermal conductivity, and chemical stability, making it resistant to high-temperature corrosion. However, pure phase ZrO_2 undergoes a temperature-dependent phase transition from monoclinic (m) \rightarrow tetragonal (t) \rightarrow cubic (c), with the reverse process taking place upon cooling. This non-diffusion martensite phase transition process occurs rapidly during cooling, causing approximately 3.5% volume expansion, equivalent to a reduction in theoretical density from 6.1 to 5.9 g/cm^3 . Therefore, pure phase ZrO_2 is not suitable for thermal barrier coating applications [6–10] (Fig. 1).

To enhance the comprehensive properties of ZrO_2 ceramics and mitigate phase transition defects, stabilizers such as magnesium oxide (MgO), calcium oxide (CaO), yttrium oxide (Y_2O_3), cerium oxide (CeO_2), and others are used [12–14]. The addition of tetravalent oxides, such as MgO, generates oxygen vacancies through charge balance, while cation substitution defects in the ZrO_2 ceramic lattice play a secondary role. 7–8 wt% yttria-stabilized zirconia (7YSZ) is widely used for thermal barrier coatings due to its intrinsic low thermal conductivity (about 2.5 W/(m k)), high thermal expansion coefficient (about $10\text{--}11 \times 10^{-6} \text{ K}^{-1}$), high hardness (about 10 GPa), and low elastic modulus (about 220 GPa), exhibiting improved comprehensive performance at high temperatures up to 900 °C [15].

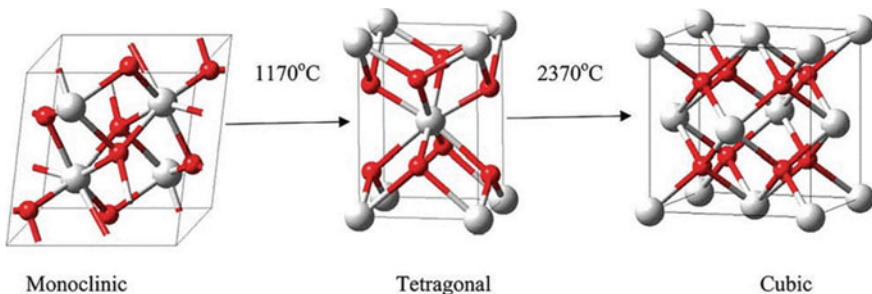


Fig. 1 Zirconia allotropes and the phase transformation temperature [11]

1.2 Effect of Doping Modification on Materials

The incorporation of Y_2O_3 in zirconia has been found to prevent the $t' \rightarrow m$ phase transition in zirconia. When the mass fraction of Y_2O_3 exceeds 22%, zirconia is fully stabilized into the cubic phase at room temperature, which is referred to as yttria completely stabilized zirconia [16]. Alternatively, when the mass fraction of Y_2O_3 is less than 22%, zirconia can be partially stabilized into the tetragonal phase (8–22% mass fraction) or the metastable tetragonal phase (6–8% mass fraction) depending on the stabilizer used, and this is referred to as yttria partially stabilized zirconia. At present, stable ZrO_2 with a Y_2O_3 mass fraction ranging from 6 to 8%, denoted as 6–8YSZ, is the most commonly used material for various applications including thermal barrier coatings. Metastable tetragonal 6–8YSZ exhibits excellent fracture toughness ($1.85\text{--}2.23 \text{ MPa m}^{1/2}$), good thermal insulation properties ($2.1 \text{ W m}^{-1} \text{ K}^{-1}$), a thermal expansion coefficient ($10.5\text{--}11.5 \times 10^{-6} \text{ K}^{-1}$) that is similar to that of metal bonding layers, and good corrosion resistance [16, 17]. Coatings prepared using the air plasma Spraying (APS) method by Zhang et al. did not exhibit any phase transitions after oxygenation at $900 \text{ }^\circ\text{C}$ for 100 h, and the coatings retained their metastable tetragonal and cubic phases. To investigate the effect of the thickness of the ceramic layer on the thermal shock performance of the YSZ coating, researchers prepared three thermal barrier coating systems using the APS method with a top thickness of 8YSZ on an Inconel 718 superalloy matrix. The thermal shock life of the coatings at $1000 \text{ }^\circ\text{C}$ was analyzed, and it was found that the coating life decreased with increasing thickness of the top ceramic layer. This is likely due to an increase in the deposition time of the coating with increasing thickness, leading to the accumulation of residual stress, microcracks, and pores in the coating, which reduce its thermal shock performance. Thick coatings tend to accumulate more residual stress during the deposition process, leading to the presence of more microcracks and pores in the prepared coating. During thermal shock tests, such residual stress may be released through crack expansion, causing thick coatings to experience cracked connections, which eventually leads to their detachment. While YSZ has excellent thermophysical properties and is widely used in thermal barrier coatings, high temperatures above $1200 \text{ }^\circ\text{C}$ can cause t' phase zirconia to transform into m phase, along with a volume expansion that creates significant internal stress and cracks within the coating. This situation provides an entry point for oxygen and molten corrosion, speeding up the internal corrosion of the coating and shortening its service life. Additionally, the sintering rate of YSZ increases at high temperatures, resulting in reduced porosity of the coating and decreased thermal insulation performance, while also weakening phonon scattering. Moreover, sintering increases the elastic modulus of the coating, reduces its crack stability, and accelerates crack propagation [18]. As a replacement material for YSZ, YGYZ refers to YSZ doped with Yb_2O_3 and Gd_2O_3 as stabilizers. Compared to YSZ, YGYZ exhibits improved oxidation resistance, sintering resistance, higher corrosion resistance, better high-temperature phase stability, and lower thermal conductivity, particularly at high temperatures where the thermal conductivity of YGYZ is only 1.24 W/(m K) . Researchers conducted an analysis of the

$\text{Na}_2\text{SO}_4 + \text{V}_2\text{O}_5$ corrosion behavior of APS-prepared YGYZ coating at 1100 °C and found that the coating exhibited good corrosion resistance and phase stability, retaining a high tetragonal phase even after 20 h of corrosion, with a degraded coating 40% less than that of YSZ. However, YGYZ has a low thermal expansion coefficient of only $9\text{--}10 \times 10^{-6} \text{ K}^{-1}$, which is much lower than the thermal expansion coefficient of nickel-based bonding layers ($15.0 \times 10^{-6} \text{ K}^{-1}$). The significant difference in thermal expansion coefficient makes it unsuitable to directly prepare YGYZ on the bonding layer as the top ceramic layer, and its fracture toughness is quite low, ranging from only 0.95–1.25 MPa m^{1/2}, making the coating susceptible to cracking easily in high-temperature working environments. To enhance the feasibility of YGYZ as an optimal ceramic layer material, Jung et al. [19] devised a high-purity YSZ buffer layer situated between the nickel-based bonding layer and the superior YGYZ ceramic layer to mitigate thermal expansion discrepancies and alleviate mismatch stress. The findings demonstrate that the YGYZ coating with high-purity YSZ buffer layer exhibited 2000 cycles in the jet engine test, which is significantly higher than those without buffer layer, ranging from 350 to 678 cycles, and higher than those with conventionally purified YSZ buffer layer, which ranged from 1127 to 1130 cycles. ScYSZ denotes YSZ doped with Sc₂O₃ as a stabilizer. Given that doping zirconia with Sc does not cause notable lattice distortion owing to its small ionic radius, the researchers opted to alter the Sc₂O₃ doping content to modify the performance of ScYSZ coating. Liu et al. [20] analyzed the phase composition of the ScYSZ coating with 8.0 mol% Sc₂O₃ after heat treatment at 1500 °C for 10 h, and the results showed that the ScYSZ coating after heat treatment was still a single non-transformable tetragonal phase. Under the same conditions, the content fraction of monoclinic phase in YSZ coating reaches 49.4 mol%, and its excellent high-temperature phase stability enables it to be applied in higher temperature environments. Fan et al. [21] studied the thermal shock life of ScYSZ coating at 1300 °C when the content fraction of Sc₂O₃ is 7 mol%. Although the doping of Sc element slightly reduces its fracture toughness ($(4.3 \pm 0.3) \text{ MPa m}^{1/2}$), its good t' phase stability and high comprehensive performance. As a result, it still has an extremely high thermal cycle life, up to 2.6 times that of YSZ coating. Although numerous studies have reported on zirconia or YSZ doped with rare earth elements, few have investigated the doping mechanism, the effect of doping content on coating properties, or the impact of different preparation methods on doped powder. With the development of nano-sized powders, the properties of nanostructured doped coatings are one of the important research directions (Fig. 2).

1.3 Preparation and Properties of YSZ TBCs

There are many preparation processes for thermal barrier coatings, mainly including thermal spraying [22], electron beam physical vapor deposition (EB-PVD) [23], chemical vapor deposition (CVD) [24], etc. Thermal spraying technologies include supersonic flame spraying (HVOF) [25], atmospheric plasma spraying (APS) [26],

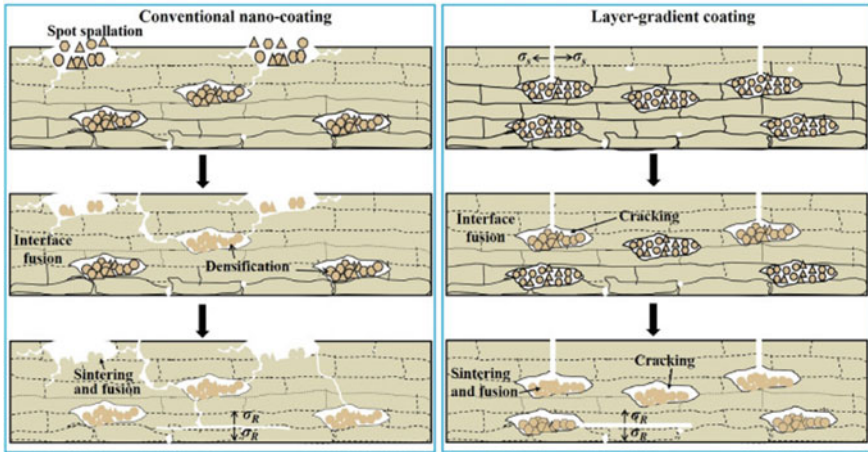


Fig. 2 Failure mechanisms of different coatings during the thermal cycling test [21]

low-pressure plasma spraying (LPPS), and the latest plasmon sprayed physical vapor deposition (PS PVD), which combines the advantages of both plasma spraying (PS) and EB-PVD [27, 28]. APS and EB-PVD spraying technologies are mainly introduced here.

Atmospheric plasma spraying is a prevalent method for preparing ceramic thermal barrier coatings due to its rapid deposition rate and cost-effectiveness [29]. Because the plasma flame flow temperature is very high, can melt most materials including metals and ceramics, atmospheric plasma spraying has a wide range of applications. Since plasma spraying involves rapid heating and cooling processes, it has a small heat-affected zone on the substrate, and some amorphous and nanocrystals may be produced in the sprayed coating [30, 31]. Figure 3 illustrates the atmospheric plasma spraying process [29]. The working gas, usually Ar and H₂/N₂, creates an arc between the cathode and anode, and the working gas is ionized to produce a plasma arc. Plasma arc has the characteristics of high temperature and high speed. In atmospheric plasma spraying, carrier gas transports the spraying powder into the plasma flame flow, where it is heated to a melting or semi-melting state. The high-speed plasma flame flow impacts the substrate surface, forming a coating. Spraying parameters such as power, plasma gas composition, and spraying distance affect the powder’s melting state, particle speed, and coating microstructure. The resulting coating has a layered structure with pores and cracks. While pores reduce thermal conductivity, cracks decrease thermal cycle life.

Advancements in nanotechnology have enabled the preparation of nanostructured thermal barrier coatings through atmospheric plasma spraying. Plasma spraying of nanostructured thermal barrier coatings has become a significant method for producing high-performance thermal barrier coatings [24, 32, 33]. By controlling spraying parameters, part of the nanostructured feed is retained in the coating without melting or partially melting to form the nanostructured coating.

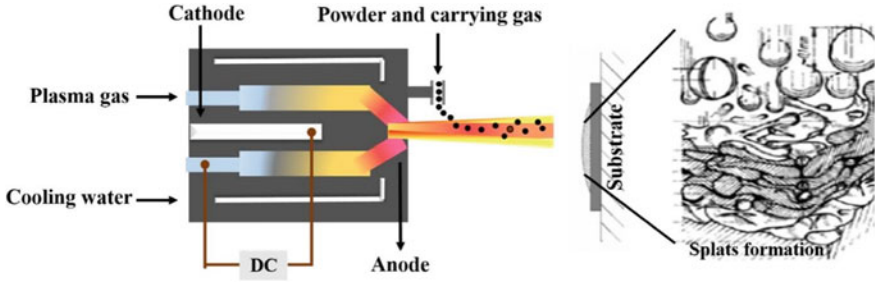


Fig. 3 Schematic diagram of atmospheric plasma spraying [29]

EB-PVD heats the target with a high-energy electron beam to vaporize it, then deposits gas-phase atoms on the substrate surface to form a coating, as illustrated in Fig. 4 [34]. The microstructure of thermal barrier coating prepared by EB-PVD is columnar crystal. Compared with APS coating, EB-PVD coatings exhibit greater strain tolerance, compactness, and bonding strength. However, its thermal conductivity is relatively high, deposition rate is slow, and cost is high.

PS-PVD is a recently developed technology for preparing thermal barrier coatings that challenges traditional understanding of plasma spraying. In an ultra-low-pressure environment (pressure of about 50–200 Pa), a large power (up to 130 kW) spray gun is used to generate a plasma flame with a length of 2 m and a diameter of 0.2–0.4 m, as shown in Fig. 5 [35]. PS-PVD enables solid, liquid, and gas multiphase deposition as well as non-line-of-sight deposition. By adjusting spraying

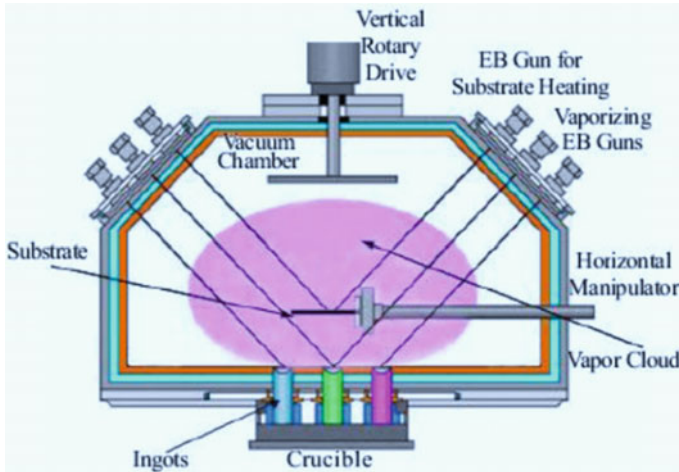


Fig. 4 Schematic diagram of EB-PVD [34]

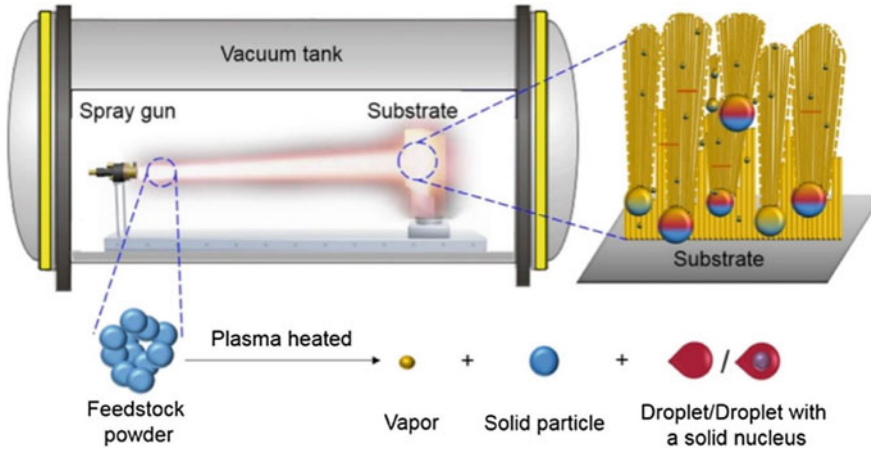


Fig. 5 Plasma jet of PS-PVD [35]

parameters, thermal barrier coatings with layered, columnar, and layered structures can be obtained. Therefore, as an advanced thermal barrier coating preparation technology, PS-PVD holds significant potential for future preparation of high-performance high-temperature and ultra-high-temperature thermal barrier coatings [36, 37].

Yttrium oxide-stabilized zirconia (6–8YSZ) with a mass fraction of 6–8% is the most excellent and widely used thermal barrier coating material at present. YSZ has advantages such as high melting point ($\sim 2700\text{ }^{\circ}\text{C}$), low thermal conductivity ($2\text{--}3\text{ W m}^{-1}\text{ K}^{-1}$), high thermal expansion coefficient ($\sim 11.0 \times 10^{-6}\text{ K}^{-1}$), excellent chemical stability at high temperature and comprehensive mechanical properties. In particular, its excellent toughness at high temperature is incomparable to other thermal barrier coating materials. The fracture toughness of YSZ can reach $3\text{ MPa m}^{1/2}$, which is related to the ferroelastic toughening mechanism existing in t, the metastable tetragonal phase of YSZ. t phase usually only exists in YSZ coating prepared by atmospheric plasma spraying or electron beams-physical gas deposition.

The T' phase is a metastable phase between the T and C phases. Unlike the T phase, the T' phase does not undergo a transformation to the M phase, enhancing YSZ's phase stability and preventing volume expansion caused by martensitic transition. In addition, t-phase YSZ is also a kind of ferroelastic material with excellent fracture toughness at high temperature. Under the action of stress, long strip domain structure, called ferroelastic domain, will be formed in the grain. In the t' phase, the ferroelastic domain structure will be deflected under the action of stress, from the original along $\langle 111 \rangle$ superlattice crystal faces stacked in the direction and containing only a single orientation are transformed into superlattice faces containing three orientations parallel to axes a, b, and c, respectively. The steering process is shown in 1.6 (a) 34. The nucleation and steering of ferroelastic domains will absorb part of the energy

of crack growth, slow down the rate of crack growth, cause stress–strain hysteresis effect, and thus, improve the fracture toughness of YSZ.

As engine service temperatures increase, the corrosion of thermal barrier coatings by CMAS ($\text{CaO-MgO-Al}_2\text{O}_3\text{-SiO}_2$) becomes more severe. Shan et al. [38] studied the buckling of plasma-sprayed YSZ thermal barrier coatings under CMAS erosion and its induced effects. At high temperature, the liquid CMAS permeates the weakened interface into the YSZ due to capillary force and makes the YSZ expand significantly by about 32%, resulting in a wide range of YSZ buckling. To demonstrate the process, baseless APS TBC coated with CMAS were prepared and heated to 1250 °C in a tubular furnace. Figure 6a shows the buckling process of TBC under different heat treatment times. With the increase of holding time, the penetration depth of CMAS increases, and the buckling becomes more obvious. Based on the discussion, the buckling failure mechanism of TBC under the action of CMAS is proposed, as shown in Fig. 6b. Thornton et al. [39] found that molten CMAS increased mass transport in YSZ coatings prepared by APS and EB-PVD, leading to densification and peeling during cooling. Increased mass transport can destabilize the YSZ coating by incorporating stabilizers and precipitating the zircon phase. Finally, the corrosion failure mechanism of CMAS coating is proposed, namely “penetration, dissolution, densification, precipitation, and spalling”.

Despite its advantages as a thermal barrier coating material, YSZ has limitations. As aero-engine technology advances, YSZ’s shortcomings become more apparent. When the service temperature exceeds 1200 °C, the T phase dissolves into the C and T’ phases, reducing the coating’s fracture toughness. Increased T phase content

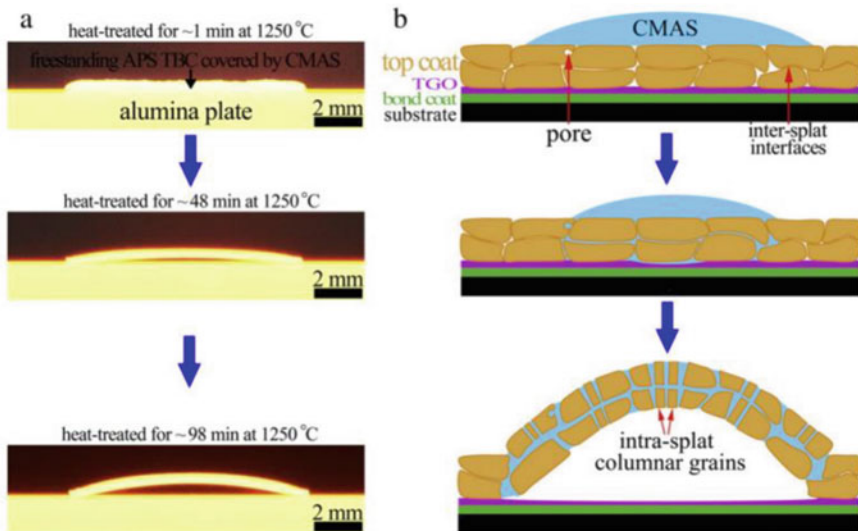


Fig. 6 a Buckling failure processes of APS TBC with CMAS at 1250 °C and b schematic illustration of buckling failure mechanism of APS TBC after CMAS attack

exacerbates volume expansion caused by the $T \rightarrow M$ phase transition, leading to cracking and coating detachment. Thus, YSZ's working temperature is limited to below 1200 °C. In addition, as an excellent conductor of oxygen ions, YSZ is usually used as electrode material for solid batteries. In particular, YSZ has a very high permeability of oxygen ions at high temperature, which will accelerate the oxidation of metal bonding layer to form TGO. Problems such as poor sintering resistance, high thermal conductivity, and poor corrosion resistance also greatly limit the application of YSZ thermal barrier coating on high-performance aero-engines. Therefore, to find a new thermal barrier coating material that can replace YSZ has become the focus of research.

1.4 Application of Hafnium Oxide in TBCs

In the top thermal barrier layer, hafnium exists as HfO_2 , stabilized by yttrium or other rare earth oxides. Alternatively, hafnium dioxide can be used as an additive to conventional coatings that stabilize ZrO_2 . Common techniques for applying hafnium dioxide thermal barrier coatings include electron beam physical vapor deposition (EB-PVD), air plasma spray (APS), and magnetron sputtering. When HfO_2 is stabilized with 27 wt% Y_2O_3 , it exhibits reduced Young's modulus and thermal conductivity (by 30% to 0.5–1 W/(m K)) at high temperatures, resulting in higher sintering resistance and heat resistance compared to 8YSZ coating. Doping ZrO_2 and HfO_2 with a mixture of trivalent ions larger and smaller than Y^{3+} maintains the metastable t' phase structure. Phase diagrams are crucial for selecting surface components and doping elements of the adhesive coating. Adding up to 1 wt% hafnium to the bonded coating improves its cyclic oxidation resistance and increases the adhesion and strength of the hot-growing oxide layer to the bonded coating.

2 Rare Earth Zirconate

2.1 Crystal Structure of Rare Earth Zirconate in TBCs

Rare earth zirconates ($Ln_2Zr_2O_7$) include ordered pyrochloitic structures and disordered defect fluorite structures. The transformation of two structures under normal temperature and pressure is dependent on the Ln^{3+}/Zr^{4+} cation radius ratio. An ordered pyrochloitic structure of $Ln_2Zr_2O_7$ occurs when the Ln^{3+}/Zr^{4+} radius ratio is between 1.46 and 1.78. A disordered defective fluorite structure occurs when the ratio is less than 1.46. The general formula for the pyrochloitic structure of rare earth zirconate is $Ln_2Zr_2O_6O'$, which belongs to the $Fd\bar{3}m$ space group with ordered Ln^{3+}/Zr^{4+} cations. Its single cell structure is shown in Fig. 7a. This structure has four crystallographic inequivalent atomic positions, namely Ln^{3+} occupying the 16d

space position and Ln^{3+} occupying the 16d space position. It can coordinate with the surrounding eight oxygen ions to form a cube. Zr^{4+} at position 16c, together with six surrounding oxygen ions, forms an octahedral structure. The oxygen ion O at position 48f, and the oxygen ion O' at position ④8b. In addition, the oxygen vacancy at position 8a in Fig. 7a, which is in the tetrahedron formed by Zr^{4+} , also shows ordering. The general formula of the disorder defect fluorite type rare earth zirconate is $(\text{Ln}, \text{Zr})_4\text{O}_7$ and belongs to the $\text{Fm}\bar{3}\text{m}$ space group, as shown in Fig. 7b. The Ln^{3+} , Zr^{4+} cations share a crystallographic position 4a, and the oxygen ions only have a crystallographic position 8c. The structure also has 1/8 oxygen ion vacancies. It is caused by the random distribution of equivalent crystallographic positions, and the position of oxygen vacancies is also randomly distributed. Rare earth zirconate has an oxygen vacancy in each molecular unit, so its lattice has a high oxygen vacancy concentration. Ln^{3+} and Zr^{4+} can be substituted by various cations with similar atomic radii. The material's complex unit cell structure and large rare earth atoms result in a high melting point, low thermal conductivity, and high chemical stability. It has been extensively studied in the field of TBCs and is expected to become a candidate for new TBCs.

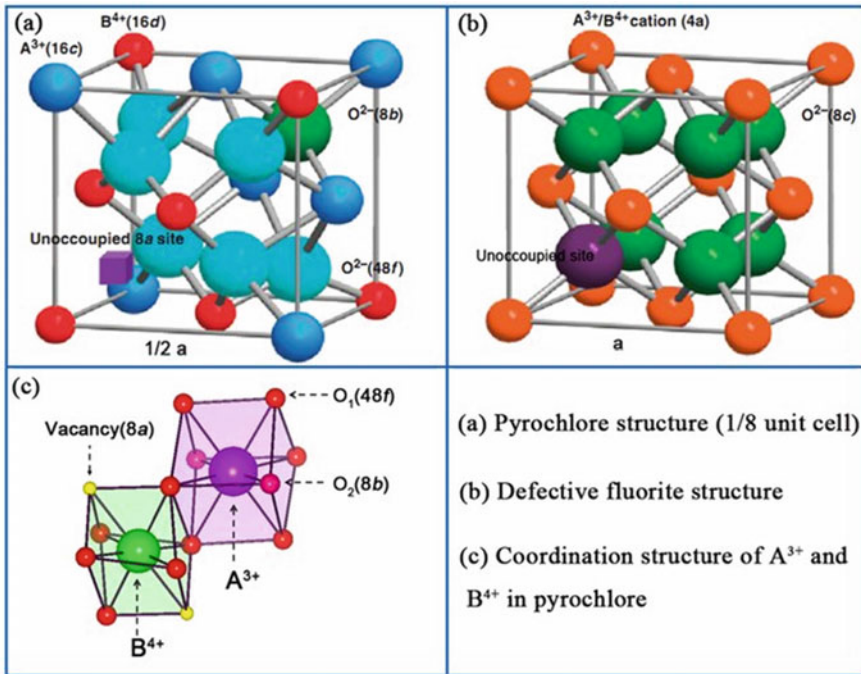


Fig. 7 Crystal structures of pyrochlore and defective fluorite: **a** one-eighth of unit cell of pyrochlore structure; **b** defective fluorite structure; **c** coordination structure of A^{3+} and B^{4+} in pyrochlore [40]

2.2 Properties of Rare Earth Zirconate TBCs

Rare earth zirconate is a promising thermal barrier coating (TBC) material due to its high phase stability, low thermal conductivity, anti-sintering properties, and low oxygen transmittance. It is particularly resistant to CMAS corrosion.

Rare earth zirconate materials have intrinsic oxygen vacancies in each crystal structure unit, whether it is a pyrochlore or defect fluorite structure. The high concentration of oxygen vacancies and the presence of large rare earth atoms in the unit cell enhance phonon scattering and decrease the mean free path, resulting in low thermal conductivity. While there are variations in thermal conductivity due to differences in preparation processes, material porosity, and testing conditions, these materials generally have lower thermal conductivity than conventional YSZ under the same conditions. Their thermal expansion coefficient is equivalent to or slightly lower than that of YSZ.

As a potential new type of thermal barrier coating, rare earth zirconate thermal barrier coating, its high-temperature corrosion resistance in $\text{Na}_2\text{SO}_4\text{-V}_2\text{O}_5$ environment, and the ability to resist the corrosion of $\text{CaO-MgO-Al}_2\text{O}_3\text{-SiO}_2$ (CMAS) are also the main goals of TBCs development. Kramer et al. [41] used the electron beam physical vapor deposition method to prepare $\text{Gd}_2\text{Zr}_2\text{O}_7$ coating. After coating the surface of $\text{Gd}_2\text{Zr}_2\text{O}_7$ with CMAS molten salt ($33\text{CaO-9MgO-13AlO}_{3/2}\text{-45SiO}_2$) at a concentration of 8 mg/cm^2 and holding it at 1573 K for 4 h , a dense fine-grained reaction layer with a thickness of about $6\text{ }\mu\text{m}$ was formed at the interface between the $\text{Gd}_2\text{Zr}_2\text{O}_7$ coating and CMAS. The reaction layer is mainly composed of $\text{Gd}_2\text{Ca}_2(\text{SiO}_4)_6\text{O}_2$ apatite phase and ZrO_2 fluorite phase with solid solution of Gd and Ca. This study shows that the depth of the CMAS molten salt penetrating into the cylindrical crystal gap of the ceramic layer is about $30\text{ }\mu\text{m}$. When the cylindrical crystal gap is filled with the generated product and molten salt, the molten salt infiltration will stop, and then, the top of the cylindrical crystal will be slowly eroded.

Our research group used EB PVD to deposit YSZ and LZ7C3 coatings on ceramic substrates and studied their high-temperature CMAS behavior at $1250\text{ }^\circ\text{C}$. It was found that the LZ7C3 coating was highly resistant to CMAS penetration within 24 h , while the conventional YSZ was completely permeated by the CMAS melt within 30 min . This resistance is mainly due to the high-temperature chemical interaction between the LZ7C3 coating and CMAS glass, which crystallizes to form a protective layer. The crystallization product is primarily composed of La Ce apatite and cubic phase ZrO_2 , which can form a closed layer that effectively prevents further CMAS penetration. This is mainly due to the high-temperature chemical interaction between the LZ7C3 coating and the CMAS glass, which crystallizes to form this resistance. The crystallization product is mainly composed of La Ce apatite and cubic phase ZrO_2 , which is easy to form a closed layer and can effectively prevent further penetration of CMAS.

2.3 Modification of Rare Earth Zirconate

Rare earth zirconate $\text{La}_2\text{Zr}_2\text{O}_7$ is used in thermal barrier coatings (TBCs) due to its thermal expansion coefficient being close to that of the currently used TBC material YSZ, its lower thermal conductivity, and higher phase stability. However, $\text{La}_2\text{Zr}_2\text{O}_7$ has some shortcomings, such as insufficient sintering activity, poor thermal cycle performance, and high-temperature thermal radiation that increases thermal conductivity. To reduce the thermal conductivity of TBC ceramics, researchers have doped them with different rare earth elements or other stabilizers to improve their performance. In recent years, a series of complex rare earth zirconates with varying thermal and mechanical properties have been obtained by doping zirconates with rare earth elements, such as $(\text{La}_x\text{Gd}_{1-x})_2\text{Zr}_2\text{O}_7$, $(\text{Sm}_x\text{Yb}_{1-x})_2\text{Zr}_2\text{O}_7$, $(\text{La}_x\text{Yb}_{1-x})_2\text{Zr}_2\text{O}_7$, and $(\text{La}_x\text{Gd}_{1-x})_2\text{Zr}_2\text{O}_7$, $\text{Gd}_2(\text{Zr}_x\text{Ti}_{1-x})_2\text{O}_7$, $(\text{Sm}_{2-x}\text{Mg}_x)_2\text{Zr}_2\text{O}_{7-x/2}$, $\text{La}_2(\text{Zr}_x\text{Ce}_{1-x})_2\text{O}_7$ and further reduce the thermal conductivity of the system, while obtaining a higher thermal expansion coefficient. The following are some studies on the doping of $\text{La}_2\text{Zr}_2\text{O}_7$.

(1) Single doping of rare earth elements forms rare earth zirconate

Wang et al. [42] doped $\text{La}_2\text{Zr}_2\text{O}_7$ with Nd oxide (Nd_2O_3) to form $\text{La}_{2-x}\text{Nd}_x\text{Zr}_2\text{O}_7$ ceramic materials, and $\text{La}_{1.4}\text{Nd}_{0.6}\text{Zr}_2\text{O}_7$ has the lowest coefficient of thermal expansion ($8.928 \times 10^{-6} \text{ K}^{-1}$) and the best anti-sintering performance. Good anti-sintering ability reduces the thermal effect force between the ceramic coating and metal substrate, which is crucial for thermal barrier coating (TBC) materials. Lehmann et al. [43] Nd_2O_3 , Eu_2O_3 , Gd_2O_3 , Dy_2O_3 doped $\text{La}_2\text{Zr}_2\text{O}_7$ formed $\text{La}_{1.4}\text{Nd}_{0.6}\text{Zr}_2\text{O}_7$, $\text{La}_{1.4}\text{Eu}_{0.6}\text{Zr}_2\text{O}_7$. The thermal conductivity of $\text{La}_{1.4}\text{Gd}_{0.6}\text{Zr}_2\text{O}_7$ and $\text{La}_{1.7}\text{Dy}_{0.3}\text{Zr}_2\text{O}_7$ is lower than that of $\text{La}_2\text{Zr}_2\text{O}_7$, which is $1.55 \text{ W}/(\text{m K})$. Therefore, the doping of rare earth oxide can improve the performance of thermal barrier coating materials. The thermal conductivity of $\text{La}_{1.4}\text{Gd}_{0.6}\text{Zr}_2\text{O}_7$ and $\text{La}_{1.7}\text{Dy}_{0.3}\text{Zr}_2\text{O}_7$ is lower than that of $\text{La}_2\text{Zr}_2\text{O}_7$ ($1.55 \text{ W}/(\text{m K})$), indicating that doping with rare earth oxide can improve the performance of thermal barrier coating materials. Wan et al. [44] found that $\text{La}_{1.4}\text{Gd}_{0.6}\text{Zr}_2\text{O}_7$ had lower thermal diffusivity and conductivity than undoped rare earth misate ceramic material. Replacing La with other rare earth ions weakens the La–O bond and facilitates its expansion, improving the thermal expansion coefficient of zirconate. Studies on Gd_2O_3 -doped $\text{La}_2\text{Zr}_2\text{O}_7$ ($\text{La}_{1.7}\text{Dy}_{0.3}\text{Zr}_2\text{O}_7$, $\text{La}_{1.7}\text{Yb}_{0.3}\text{Zr}_2\text{O}_7$, and $\text{La}_{1.7}\text{Yb}_{0.15}\text{Gd}_{0.15}\text{Zr}_2\text{O}_7$) showed lower thermal conductivity than undoped $\text{La}_2\text{Zr}_2\text{O}_7$ due to strong phonon scattering caused by the vibration of 3-valent rare earth ions with smaller ion radius and larger mass in the original lattice. Thus, doping $\text{La}_2\text{Zr}_2\text{O}_7$ with active ions with small ion radius and large mass can achieve lower thermal conductivity.

Wan et al. [45] studied Yb_2O_3 doped with $\text{La}_2\text{Zr}_2\text{O}_7$, and in the system of $(\text{La}_x\text{Yb}_{1-x})_2\text{Zr}_2\text{O}_7$, Yb^{3+} with smaller radius was doped instead of La^{3+} with larger radius, which caused strong vibration of atoms at this position and reduced the phonon mean free path equals the level of nearest neighbor atomic spacing during heat conduction, which significantly decreased low material thermal conductivity,

different from the traditional YSZ thermal barrier coating phase transition aging, the phase transition process of $\text{LaYb}_2\text{Zr}_2\text{O}_7$ is relatively slow, and there is no huge mismatch between components or the generation of new phases that can induce catastrophic consequences. The phases involved in the phase transition have a high similarity, and the two new phases can coexist stably at high temperature for a long time. These characteristics make $\text{LaYb}_2\text{Zr}_2\text{O}_7$ a promising candidate for use as a thermal barrier coating material.

(2) Zr position in rare earth element doped zirconate ($\text{La}_2\text{Zr}_2\text{O}_7$)

In thermal insulation materials such as ceramics, the thermal conductivity is mainly affected by phonons, so if the elements with large ionic radius and large relative atomic mass are doped in the material, the thermal conductivity will naturally decrease. The ease of doping and the decrease in thermal conductivity of a system are influenced by the difference between the ionic radius and average atomic mass of doped and raw material atoms. Ce^{4+} has a larger ionic radius and relative atomic mass than Zr^{4+} , making it beneficial to replace Zr^{4+} with Ce^{4+} in lanthanum zirconate to improve its thermal expansion coefficient and reduce its thermal conductivity. Cao et al. [46] studied the thermal properties of $\text{La}_2(\text{Zr}_{1-x}\text{Ce}_x)_2\text{O}_7$ thermal barrier coating material and found that the addition of CeO_2 significantly increased the thermal expansion coefficient of $\text{La}_2\text{Zr}_2\text{O}_7$ due to the large ionic radius of Ce^{4+} and weak Ce–O bond energy. The thermal conductivity also decreased significantly due to the complex crystal structure reducing the mean free path of phonons. At 1000 °C, $\text{La}_2(\text{Zr}_{0.7}\text{Ce}_{0.3})_2\text{O}_7$ ceramic material had the lowest thermal conductivity ($0.87 \text{ W m}^{-1} \text{ K}^{-1}$) and best sintering resistance, improving its thermal stability. No phase transition occurred below 1200 °C, and at 1200 °C its thermal conductivity and thermal expansion coefficient were $0.79 \text{ W m}^{-1} \text{ K}^{-1}$ and $11.6 \times 10^{-6} \text{ K}^{-1}$, respectively, representing a 50% reduction and 20% increase compared to $\text{La}_2\text{Zr}_2\text{O}_7$.

(3) Double doped rare earth element modified $\text{La}_2\text{Zr}_2\text{O}_7$ ceramic material

Cao et al. [46, 47], to enhance the material's chemical and phase stability, completely or partially replaced La_2O_3 with Y_2O_3 , and the products after substitution included $\text{Y}_2\text{Ce}_2\text{O}_7$, $\text{Y}_2(\text{Zr}_{0.7}\text{Ce}_{0.3})_2\text{O}_7$, and $\text{Yb}_2(\text{Zr}_{0.7}\text{Ce}_{0.3})_2\text{O}_7$, among all the components, $\text{Y}_2\text{Ce}_2\text{O}_7$ is monophasic, and the other components are mixtures with different structures. The complete or partial substitution of Y_2O_3 for La_2O_3 resulted in a linear decrease in the unit cell parameters of the product, indicating that Y^{3+} replaced the lattice site of La^{3+} or Ce^{4+} . Of these products, LZC3 has the lowest thermal conductivity. It is also the most resistant to sintering, so it has an important application in high-temperature thermal barrier coating. The $\text{La}_{1.7}\text{Dy}_{0.3}(\text{Zr}_{0.8}\text{Ce}_{0.2})_2\text{O}_7$ and $\text{La}_{1.7}(\text{DyNd})_{0.15}(\text{Zr}_{0.8}\text{Ce}_{0.2})_2\text{O}_7$ ceramic materials studied by Zhou have good phase stability at high temperature, and no phase occurred. Consequently, there is an increase in the thermal expansion coefficient and a decrease in thermal conductivity. In comparison with non-doped $\text{La}_2\text{Zr}_2\text{O}_7$, these doped products exhibit greater suitability as high-temperature thermal barrier coating materials. Despite the fact that ion substitution can enhance its performance to a certain degree, it remains challenging

to improve the thermal expansion coefficient of $\text{La}_2\text{Zr}_2\text{O}_7$ to match that of the current thermal barrier coating 7–8YSZ. The reason is that, except for the substitution of La by light rare earth elements, the substitution of other ions is not conducive to the stability of the structure and forms a heterophase. In other words, the doped ions do not enter the Gd site of La or Zr and generate impurities; ion substitution has little effect on the specific heat capacity.

Overall, rare earth zirconate is considered the most comparable thermal barrier coating material system to yttria-stabilized zirconia due to its lower thermal conductivity, similar thermal expansion coefficient to yttria-stabilized zirconia (YSZ), and high phase stability. However, rare earth zirconate still has insufficient comprehensive mechanical properties, poor thermal cycling performance, and radiation at extremely high temperature. Thermal conductivity results in an increase in thermal conductivity and numerous other issues. Extensive research is required prior to the realization of industrial application.

2.4 Properties of Nanostructured Rare Earth Zirconate Coatings

With the development of nanotechnology, the combination of nanomaterials and plasma spraying technology makes it possible to fabricate nanostructured thermal barrier coatings by plasma spraying. By controlling the spraying parameters, the nanostructured granulating powder only partially melts before colliding and depositing with the matrix, forming a structure in which the internal solid nanoparticles are wrapped by the fully melted liquid phase, so that the final coating contains both the fully melted region and the nano-region with the morphology similar to the microscopic nanoparticles of the granulating powder. Over the past 20 years, many researchers at home and abroad have conducted a lot of research on the nanostructure YSZ thermal barrier coating. Research has demonstrated that the properties of YSZ thermal barrier coatings, when incorporating nano-regions, exhibit significant improvements compared to traditional thermal barrier coatings. These improvements include high bond strength, robust thermal shock resistance, high thermal insulation, and strong corrosion resistance. Currently, several major aviation and development enterprises in China have implemented nanostructured YSZ ceramic thermal barrier coatings.

(1) Effect on thermal conductivity

For crystalline materials, phonon heat conduction can be understood as the result of phonon–phonon, phonon–impurity, defect, and grain boundary collisions according to the phonon theory of lattice waves. The elevated concentration of oxygen vacancies in rare earth zirconate crystals results in strong phonon scattering, reducing its thermal conductivity by nearly 30% compared to YSZ. Furthermore, doping of rare earth zirconate at the Ln and Zr sites leads to an increase in oxygen vacancies and a

decrease in the mean free path of phonons, further scattering phonons and reducing the thermal conductivity of materials. As grain size decreases to the nanometer level, grain boundaries increase dramatically in nanostructured coatings. Generally, grain boundaries act as barriers to thermal conductivity, resulting in lower thermal conductivity for nano-polycrystalline materials compared to their single-crystalline counterparts and decreasing with decreasing grain size. Additionally, the uniform distribution of pores in nanostructured coatings is a significant factor contributing to low thermal conductivity.

Taleghani et al. [48] synthesized LZ7C3 nano-powder via the chemical precipitation method and subsequently fabricated a nanostructured LZ7C3/YSZ double-ceramic layer thermal barrier coating using the plasma spraying process after granulation. Results indicate that the thermal insulation capability of the nanostructured bi-ceramic barrier coating is 58.8% greater than that of traditional YSZ coatings. This enhancement in thermal insulation capability is attributed to the extensive presence of nano-regions in the top microstructure of the coated ceramic, with the existence of nanoparticles and nanopores contributing to a significant reduction in thermal conductivity.

(2) Effect on the coefficient of thermal expansion

The thermal expansion of crystalline materials arises from the non-harmonic vibration of atoms. As temperature increases, the average atomic spacing within the crystal expands, resulting in crystal expansion. The coefficient of thermal expansion is proportional to the average distance between lattice particles, with lower bond energy corresponding to larger average lattice distances and higher coefficients of thermal expansion. Kutty et al. [49] and Shimamura et al. [50] investigated the thermal expansion coefficient of rare earth zirconia $\text{Ln}_2\text{Zr}_2\text{O}_7$ ($\text{Ln} = \text{La}, \text{Nd}, \text{Sm}, \text{Eu}, \text{Gd}$) over a temperature range from room temperature to 1500 °C and discovered that the thermal expansion coefficient increased gradually with decreasing ion radius. Schelling et al. [30, 51] also summarized the thermal expansion coefficients of $\text{La}_2\text{Zr}_2\text{O}_7$, $\text{Sm}_2\text{Zr}_2\text{O}_7$ and $\text{Gd}_2\text{Zr}_2\text{O}_7$ as 9.1×10^{-6} , 10.8×10^{-6} and $11.6 \times 10^{-6} \text{ K}^{-1}$ (20–1000 °C), respectively. In the crystal structure of rare earth zirconate, the primary determinant of material expansion is the thermal expansion of Ln–O and Zr–O bonds upon heating. Fan et al. [21] found from theoretical calculations that Zr–O bond had the greatest influence on thermal expansion, followed by Ln–O bond. Research also showed that Zr-site doping was more effective than Ln site doping in improving thermal expansion coefficient. Simultaneously, doping introduces point defects into the lattice, relaxing the lattice, reducing crystal bond energy, and increasing the expansion coefficient.

Li et al. [52] synthesized $\text{La}_2\text{Zr}_2\text{O}_7$ nano-powder with an average particle size of approximately 20 nm via the sol–gel method and evaluated its thermophysical properties after high-pressure sintering into a ceramic block. Results indicated that the thermal expansion coefficient of the ceramic block prepared from $\text{La}_2\text{Zr}_2\text{O}_7$ nano-powder was $(9.6 \pm 0.4) \times 10^{-6} \text{ K}^{-1}$ (20–1000 °C), significantly higher than that of the non-nano-powder sample $(9.1 \pm 0.4) \times 10^{-6} \text{ K}^{-1}$. It was also noted that powder nanometerization is an effective means of improving the performance of

thermal barrier coatings, demonstrating the potential of nanostructured coatings in enhancing the thermal expansion coefficient of thermal barrier coatings.

The fracture toughness index of thermal barrier coatings indicates their ability to resist crack instability propagation or fracture. The nanostructure of nano-thermal barrier coatings can enhance the coating's toughness. According to Hall–Petch's equation, reducing the grain size from micrometers to nanometers can improve the material's mechanical properties. In addition, increasing grain boundaries is a method that can slow down crack propagation. In nanostructured coatings, crack propagation is easily blocked, tortuified, and deflected by the nano-regions in the coating, so that the crack propagation path in nano-thermal barrier coatings has no obvious direction. For conventional coatings with a dominant melting region, the crack propagation is clearly directional, usually along the direction of the lamellae interface. As a result, the fracture toughness of nano-coatings is higher than that of conventional coatings.

Li et al. [53] prepared $\text{La}_2\text{Zr}_2\text{O}_7$ micro and nano-powders using solid-phase and sol–gel methods and found that the fracture toughness of bulk materials prepared from nano-powder ($1.98 \pm 0.07 \text{ MPa m}^{1/2}$) was significantly higher than that of micro powder samples ($1.40 \pm 0.23 \text{ MPa m}^{1/2}$). Researchers pointed out that compared with the traditional $\text{Gd}_2\text{Zr}_2\text{O}_7$ coating that failed after 40 h oxidation at $1100 \text{ }^\circ\text{C}$ in previous studies the oxidation life of $\text{Gd}_2\text{Zr}_2\text{O}_7$ coating with nanostructure increased by more than 2 times to 100 h at $1100 \text{ }^\circ\text{C}$. The increase of the grain boundaries of the nanostructured coating leads to slower crack propagation, which has a significant effect on improving the fracture toughness and the life of the coating.

3 Rare Earth Cerate

3.1 Crystal Structure of Rare Earth Cerate in TBCs

The crystal structure of rare earth cerite $\text{RE}_2\text{Ce}_2\text{O}_7$ is similar to that of rare earth zirconate. However, due to the large ionic radius of Ce^{4+} , the ratio of the ionic radius of the A site to the B site is typically less than 1.46, resulting in a defect fluorite structure with a 1/8 oxygen vacancy. Rare earth cerates are solid solutions formed by solid solution of other kinds of rare earth oxides into the CeO_2 lattice. Therefore, they have the same cubic fluorite structure as CeO_2 . Taking lanthanum cerate (LC) as an example, it is a solid solution with La_2O_3 as the solute and CeO_2 as the solvent. In this structure, La^{3+} and Ce^{4+} occupy the 4a site together, with oxygen vacancies randomly distributed in the oxygen ion sublattice. Figure 8 shows the distribution of anions and cations in the unit cell of the ideal cubic fluorite structure (MO_2), where cations form a face-centered cubic arrangement and anions are placed in the tetrahedral center formed by cations. This special configuration endows $\text{La}_2\text{Ce}_2\text{O}_7$ with many excellent characteristics, showing good chemical stability and ionic conductivity.

Praveen [55] comparative analysis of rare earth cerate coatings of doped systems prepared by APS and SPPS. Figure 9 shows no obvious phase transition before or

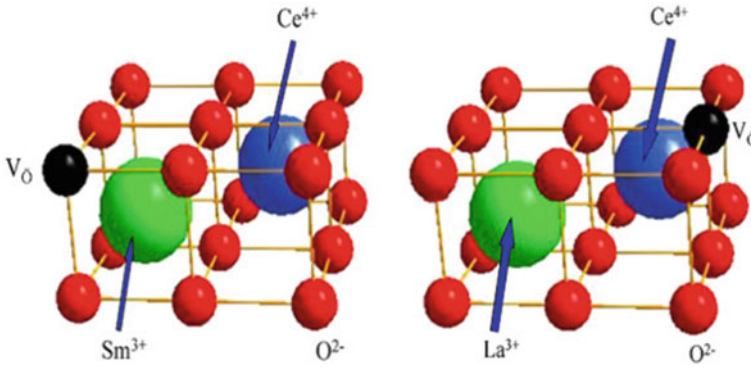
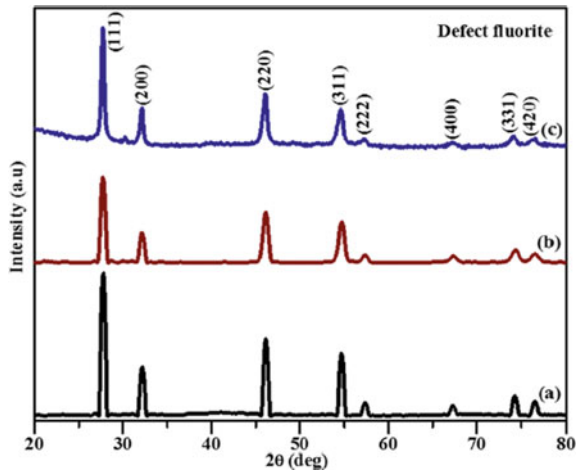


Fig. 8 Distribution of cations and anions in a fluorite cell [54]

Fig. 9 XRD pattern of a Gd-LC powder, b APS, and c SPPS coatings [55]



after APS deposition, indicating a single-phase defect fluorite structure. The SPPS coating has a prominent high peak and lower XRD intensity than synthetic powder, possibly due to the high solidification rate during plasma spraying.

3.2 Properties of Rare Earth Cerate TBCs

The rare earth cerate with fluorite structure can be understood as a solid solution generated by the dissolution of rare earth oxides in the CeO_2 lattice. CeO_2 has a low thermal conductivity and the fluorite structure's oxygen vacancies can optimize the thermal insulation performance of rare earth cerate. The large ionic radius of Ce^{4+} and weak Ce–O bond result in a high thermal expansion coefficient at high temperatures. These

properties make it a candidate for thermal barrier coatings. Researchers prepared $\text{Dy}_2\text{Ce}_2\text{O}_7$ and $\text{Y}_2\text{Ce}_2\text{O}_7$ by solid-phase reaction and measured their thermal conductivity at 800 °C to be 1.78 W/(m K) and 1.82 W/(m K), respectively, much lower than that of 8YSZ (2.15 W/(m K)) at the same temperature.

Guo et al. [56] prepared $\text{La}_2\text{Ce}_2\text{O}_7$ (LC)/yttria-stabilized zirconia (YSZ) thermal barrier coating (TBC) with a segmented crack structure using plasma spraying technology. They studied the thermal–physical properties and thermal cycling properties, such as thermal diffusivity and conductivity, of the segmented LC/YSZ TBC. The thermal conductivity of segmented coatings measured at 1200 °C was about 1.02 W/(m K), lower than that of non-segmented coatings. The thermal cycle life of segmented LC/YSZ TBC is approximately 2100 cycles, which is nearly 50% more durable than unsegmented TBC. The failure of segmented coatings is mainly due to peeling and delamination cracking inside the coating.

Researchers used $\text{La}_2\text{Ce}_{2.5}\text{O}_8$ as raw material powder to obtain $\text{La}_2\text{Ce}_2\text{O}_7$ (LC) coating close to 1 by optimizing the spraying parameters. The spraying distance significantly influences the phase composition, stability, and porosity of LC coating while keeping other spray parameters unchanged. A plasma spray coating was prepared and evaluated for thermal cycle life using a gas burner test. The thermal cycle life of LC/YSZ double-layer coatings was more than 3 times that of single-layer LC coatings and comparable to YSZ coatings at 1230 °C. At 1320 °C, the LC/YSZ coating had a thermal cycle life approximately 40% that of optimized YSZ coating but significantly lower at 1350 °C. The thermal cycling failure mechanism of LC and LC/YSZ coatings under different conditions was also established.

Researchers studied the microstructure evolution of $\text{La}_2\text{Ce}_2\text{O}_7$ (LC) and YSZ thermal barrier coatings sprayed at 1250 °C plasma. After heat treatment at 1250 °C for 12 h, the YSZ coating was severely impacted by CMAS glass-like deposition with a penetration depth exceeding 250 μm . CMAS deposition chemically reacted with LC coatings to form an interactive layer consisting mainly of $\text{Ca}_2(\text{La}_x\text{Ce}_{1-x})_8(\text{SiO}_4)_6\text{O}_{6-4x}$ and CeO_2 . The size of the interaction layer increased after 40 h of thermal exposure at 1250 °C and then remained unchanged with a thickness of <50 μm . The micro-hardness of the interaction layer after 100 h of heat exposure was about 10–12 GPa, harder than that of LC coating.

3.3 Modification of Rare Earth Cerate

Doping rare earth cerate with one or more rare earth elements can enhance the coating's performance by reducing its thermal conductivity and increasing its thermal expansion coefficient. However, in this brief introduction, the doping of Ce and Zr positions in zirconate mostly coincide.

Researchers doped Nd and La elements as dopant in $\text{Sm}_2\text{Ce}_2\text{O}_7$ and prepared $(\text{Sm}_{0.5}\text{La}_{0.1}\text{Nd}_{0.4})_2\text{Ce}_2\text{O}_7$ coating with pure fluorite structure. At 1000 °C, the thermal conductivity of the coating ranges from 1.32 to 1.58 W/(m K), while that of $\text{Sm}_2\text{Ce}_2\text{O}_7$ is 1.69 W/(m K). Doping increases the thermal expansion coefficient by

$2-3 \times 10^{-6} \text{ K}^{-1}$. According to the phonon thermal conductivity mechanism, the ion radius and relative atomic mass of the doping rare earth elements differ significantly from those in the matrix. This increases defects in rare earth cerite unit cells and reduces the coating's thermal conductivity through extra phonon scattering space.

Rare earth cerium salt exhibits excellent thermal insulation and a high thermal expansion coefficient. However, preparing lanthanum cerium coating with the rated stoichiometric ratio presents a significant challenge in its application. During plasma spraying, 30–40% of CeO_2 in rare earth lanthanum cerate is lost, resulting in a lower deposition rate for the coating. Therefore, it is necessary to increase the content of CeO_2 to obtain a prepared rare earths lanthanum cerate coating with a standard stoichiometric ratio, and the slight composition shift of CeO_2 will have a significant impact on the performance of the coating. Thermal cycling tests were carried out on the coatings with three powder doping ratios of $\text{La}_2\text{O}_3 \cdot 3.0\text{CeO}_2$ (LC3), $\text{La}_2\text{O}_3 \cdot 3.25\text{CeO}_2$ (LC3.25), and $\text{La}_2\text{O}_3 \cdot 3.5\text{CeO}_2$ (LC3.5). It was found that the composition deviation seriously affected the high-temperature life of the rare earth cerate coating. The lifetime of LC3.25 was 3238, while that of LC3 and LC3.5 was 847 and 50, respectively.

4 Rare Earth Hexaluminate

4.1 *Synthesis and Crystal Structure of Hexaluminate Materials*

Yttrium-stabilized zirconia (YSZ) is currently the most widely used TBC material, with 8% Y_2O_3 -stabilized ZrO_2 exhibiting the best thermophysical properties. However, when operating temperatures exceed 1200°C , ZrO_2 undergoes a transformation from monoclinic to tetragonal to cubic phase. This causes grain growth, microporosity shrinkage, and secondary sintering, ultimately leading to coating failure and an inability to meet the higher performance requirements of new-generation aero-engines. Therefore, it is the general trend to improve and develop new TBCs materials, so that they can work at higher temperatures for a long time, so as to meet the increasing service requirements of engines. In recent years, new TBCs materials have been emerging, and magnetic leadstone hexaluminate compounds have attracted great interest from researchers as relatively potential materials.

Hexaaluminates have a hierarchical structure consisting of alumina blocks with a spinel-like structure, separated by a single layer of symmetrical mirror planes containing large cations [57]. The crystal structure can be either β -alumina or magnetoplumbite (MP), depending on the ion radius and valence state of the metal ion. Certain metal ions can partially or completely replace aluminum. The ionic radius and charge magnitude of the metal ion determine the crystal structure. Replacement hexaaluminates may not follow the same rules as pure hexaaluminates (Fig. 10).

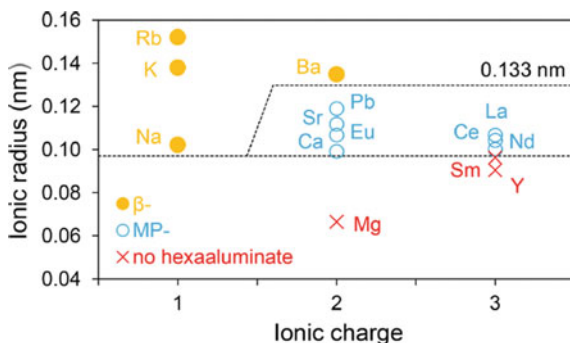


Fig. 10 Effect of charge and radius of large cation M on the formation of unsubstituted hexaaluminate [57]

The main difference between β and MP hexaaluminates is the composition and occupation of the mirror plane. In MP, the mirror plane is tightly packed, while in β it is not. The separation of spinel blocks by mirror surfaces hinders three-dimensional crystal growth, resulting in slow sintering and high stability at extreme temperatures. Crystal growth is inhibited along the C-axis to obtain a plate-like morphology with a relatively high surface area. In hexaaluminates, oxygen binds less strongly in the mirror plane than in rigid spinel blocks, making it a favorable pathway for oxide ion diffusion. This is important in catalytic applications such as combustion and selective oxidation. Alkali-containing β -HAs decompose above ~ 1000 °C in open systems due to alkali oxide vaporization, while MP-HAs with alkaline earth or rare earth cations in the mirror plane do not have this issue (Fig. 11).

In order to enhance the stability of crystal structure, some Al^{3+} ions in the crystal structure of magnetite lanthanum hexaaluminate ($LaAl_{12}O_{19}$) are usually replaced by divalent or trivalent metal cations to form $LaM_xAl_{12-x}O_{19}$ compound. When M is replaced by Mg, a magnesium-based lanthanum hexaluminate compound is formed, with the formula $LaMgAl_{11}O_{19}$ (LMA for short), which follows the principle of electric neutrality. The cell structure diagram of the material is shown in Fig. 12, which is composed of LaO_{12} decahedron containing La^{3+} ions and $(MgAl)O_4$ and AlO_6 spinel blocks separated by the mirror plane of the decahedron alternately stacked. The structural integrity of the LMA material is mainly due to the presence of orderly arranged spinel blocks reducing the $LaAl_{12}O_{19}$ cell. The cell structure diagram of the material is shown in Fig. 12. It consists of LaO_{12} decahedra containing La^{3+} ions and $(MgAl)O_4$ and AlO_6 spinel blocks separated by the mirror plane of the decahedron, stacked alternately. The structural integrity of LMA material is mainly due to the presence of orderly arranged spinel blocks reducing the $LaAl_{12}O_{19}$ cell. The void in LaO_{12} can be perfectly combined with the LaO_{12} decahedron to form stable and compact crystal structure.

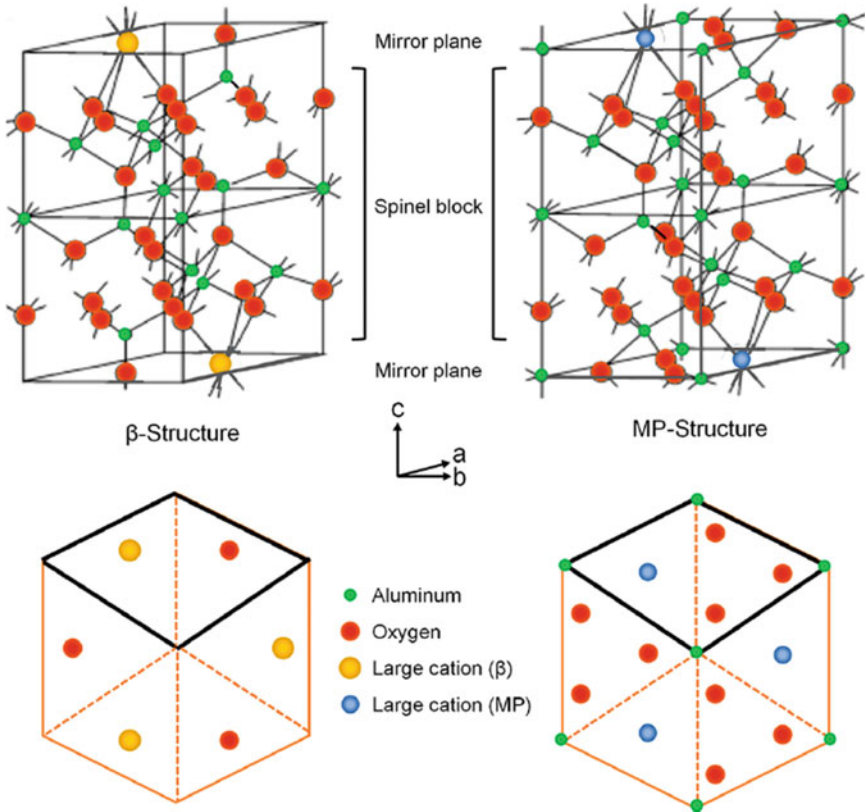
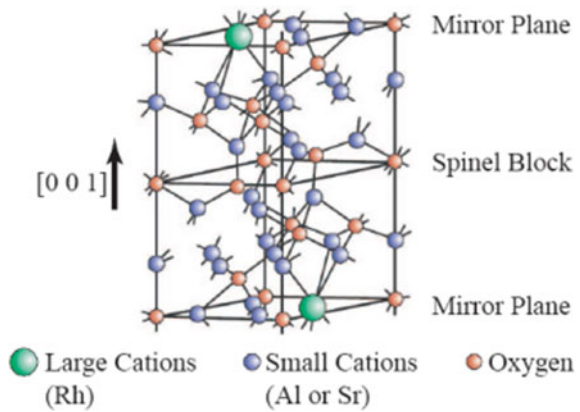


Fig. 11 Two groups of large cations depicted in Fig. 10 have an ideal hexaaluminate cell structure. The mirror plane, viewed along the C-axis, is shown below each structure. It is tightly packed in MP structures but not in β structures. In each mirror plane, the portion belonging to a cell is highlighted in bold/black [57]

Fig. 12 Schematic diagram of hexaluminate structure



The commonly used preparation methods for magnetic leadstone hexaluminate series materials mainly include solid-phase sintering method, sol-gel method, coprecipitation method, and hydrothermal method. Among them, the preparation temperature of solid-phase sintering method is high, and the calcination temperature is generally higher than 1500 °C, which has strict requirements on sintering equipment. The sol-gel method involves the hydrolysis of precursors such as alcohol salts and nitrates to generate a uniform sol, which is then converted into a gel with the assistance of an organic complexing agent. Compared to solid-phase sintering, this method reduces the crystallization temperature and produces nano-level powder material with uniform particle size and a large specific surface area. This results in improved thermal performance of the material. The material prepared by chemical coprecipitation method has the advantages of nanometer size and high purity. However, the precipitation method is more demanding on the selection of precipitant, dropping method, and dropping acceleration rate, and the aging process after precipitation takes a long time. The centrifugal filtration and cleaning process is complex, tedious, time-consuming, and labor consuming. However, the application of hydrothermal method is limited due to higher experimental conditions, greater risk coefficient, and less output.

Sol-gel method and coprecipitation method are the most commonly used methods to prepare hexaaluminate materials. The preparation process is described in detail here.

The process of preparing powder materials by sol-gel method mainly includes: the first step of metal brine hydrolysis process: the raw materials such as alkoxide and nitrate that meet the stoichiometric ratio are dissolved in the appropriate solvent, and the uniform solution is obtained by stirring and mixing for a period of time. Then there is the sol-formation process: the solution in the previous step is mixed with the appropriate and appropriate complexing agent solution, and the mixture is fully stirred to obtain a uniform mixture. Then there is the gel-forming process: the above sol is heated to obtain a thick, highly adhesive gel. It is then thoroughly dried to produce a fluffy, porous dry gel that can be easily ground into a powder. Finally, the target product was obtained after high-temperature calcination and annealing.

Coprecipitation method is to drop precipitant solution into metal salt solution, and reverse coprecipitation is to drop metal salt solution into precipitant solution. The main process of precipitation method is roughly as follows: the first is the solution preparation process: the raw materials such as carbonate and nitrate that meet the stoichiometric ratio are dissolved in the solvent together, and the salt solution is stirred evenly. Similarly, the appropriate and appropriate amount of precipitant is dissolved in the solvent, and the precipitant solution is obtained by stirring fully. Then there is the precipitation reaction process: the salt solution and the precipitant solution are titrated according to the selected method. In order to ensure the thorough reaction and obtain the fully reacted precipitate, it is required to stir while titrating, and the titration rate is as slow as possible. Then comes the aging process: after the suspension is obtained, in order to ensure that the salt ions and the precipitant are fully combined and settled, it is allowed to stand for a period of time (the standing time is related to the reaction of the material and the degree of settlement). This is followed

by the filtration process: a number of centrifugal filtrations with the appropriate cleaning solvent are carried out until the resulting filtrate has a pH value close to neutral. Finally, drying and high-temperature calcination: the cleaned precipitate is fully dried and then calcined at high temperature and annealed to obtain the target product.

4.2 Preparation and Properties of Hexaluminate TBCs

The microstructure of a material determines its performance, with variations in mechanical and thermal properties resulting from differences in microstructure. This affects the application of thermal barrier coatings (TBCs). The development of advanced coating preparation technology, which can alter the microstructure of materials, has garnered significant attention. Common TBC preparation technologies include atmospheric plasma spray (APS) and electron beam physical vapor deposition (EB-PVD), among others such as chemical vapor deposition (CVD) and high-speed flame spraying (HVOF).

Atmospheric plasma spraying (APS) is a thermal spray technology that uses plasma heating to melt powder and deposit it onto a substrate to form a thermal protective coating. APS improves the corrosion, wear, high temperature, oxidation, and fatigue resistance of the substrate. Advantages include low equipment cost, relaxed raw material requirements, fast coating preparation, and simple production. Ceramic powder is injected into the plasma flame stream and heated rapidly. Molten or partially molten particles impact the substrate at high speed. Typical APS coatings have pores and microcracks with adjustable porosity. Pores may result from non-molten particle deformation, while microcracks are related to quenching stress from rapid cooling and insufficient density of the pancake coating stack. Porosity can be adjusted by changing spraying parameters such as distance, power, and matrix temperature.

Electron beam physical vapor deposition (EB-PVD) uses electron beam energy to heat and process target material in a vacuum. The material is heated and vaporized, then deposited onto a substrate to form a protective coating. The process is environmentally friendly and produces coatings with low impurity content and consistent phase and element content. EB-PVD coatings have a columnar crystal structure with longitudinal cracks that reduce stress concentration during high-temperature service. Compared to APS coatings, EB-PVD coatings have better mechanical properties due to chemical bonding and lack of layered structure. The microstructure has higher strain tolerance and can alleviate thermal shock stress, resulting in better fatigue resistance and service life. However, EB-PVD has limitations including high cost, limited working space, inability to prepare coatings for large workpieces or complex compositions, and high pretreatment temperature for alloy matrices. Impurity elements can penetrate longitudinal cracks and erode the alloy matrix during thermal shock. Therefore, atmospheric plasma spraying is used for LMA coating preparation.

In recent decades, the research work of this material used as TBCs have been reported one after another. Its special crystal structure endows it with high-temperature phase stability and excellent electrical insulation properties, making it a promising new TBCs material for the next generation. The research progress of hexaluminate used as TBCs materials in recent years is summarized, mainly divided into the following aspects:

In addition, according to reference the intrinsic thermal conductivity of $\text{LaMgAl}_{11}\text{O}_{19}$ is lower than that of 7YSZ. The synthesized $\text{LaMgAl}_{11}\text{O}_{19}$ has no change in phase structure after heat treatment at 1600–1700 °C, indicating that the $\text{LaMgAl}_{11}\text{O}_{19}$ phase is stable below 1700 °C, which is very important for thermal barrier coatings (TBCs) at high temperature. Through SEM detection, $\text{LaMgAl}_{11}\text{O}_{19}$ has a better plate and strip structure, which improves the heat insulation and temperature resistance [58].

Phase, microstructure and thermodynamic properties of LMA pure phase materials; Sun et al. [59, 60] studied the microstructure, thermal/mechanical properties, thermal cycling and aging process at high temperatures, and crystallization mechanism of amorphous phase of LMA materials. The former found LMA ceramics from 200 to 1200 °C The linear thermal expansion coefficient at 1000 °C is $9.17 \times 10 \text{ K}^{-1}$, and the thermal conductivity at 1000 °C is 2.55 W/(m K). The latter found that the content of the amorphous phase of the LMA coating would increase with the increase of spraying power, thereby reducing the porosity of the coating, making the volume shrinkage of the coating larger and the thermal expansion coefficient lower. Sun also studied the thermal cycling behavior of the LMA coating at 1100 °C and found that the spallation of TBCs was mainly related to the formation of thermally grown oxide (TGO) and the mismatch of the thermal expansion coefficient between the coating and the matrix. It was proved that the lower the amorphous phase content of the LMA coating, the higher the bond strength with the adhesive layer, thus prolonging the service life and further crystallization of the amorphous phase The mechanism was investigated, and it was found that the highly charged La^{3+} ions in the LMA magnetite structure controlled the crystallization rate of the material, that is, the higher the La^{3+} content in the material, the more difficult the crystallization transition from multiphase to monophasic is to proceed.

Study on the erosion and high-temperature degradation mechanism of LMA materials by molten $\text{CaO-MgO-Al}_2\text{O}_3\text{-SiO}_2$ (CMAS) deposits and $\text{Na}_2\text{SO}_4 + \text{V}_2\text{O}_5$ molten salts had been carried out. Chen et al. [61] found that the microstructure and thermal properties of LMA coating are very similar to those of LMA block obtained by sintering, and the LMA coating and ceramic green body can withstand thermal corrosion for 60 h at 950 °C in the high-temperature molten salt of 50 wt% $\text{Na}_2\text{SO}_4 + 50 \text{ wt}\% \text{V}_2\text{O}_5$ without falling off. The mechanism by which molten CMAS deposits corrode thermal barrier coatings and promote their degradation at high temperature was studied and be found that a dissolution–reprecipitation reaction process would occur between LMA ceramic coatings and molten CMAS, in which $\text{CaAl}_2\text{Si}_2\text{O}_8$ and $\text{Ca}(\text{Mg, Al})(\text{Al, Si})_2\text{O}_6$ mixture, which is highly corrosive and will severely corrode the LMA coating and cause cracking and exfoliation of the coating.

LMA was synthesized with YSZ, $(\text{Yb}, \text{Er})_2\text{SiO}_5$, and $\text{Yb}_3\text{Al}_5\text{O}_{12}$. The study of the novel functional gradient TBCs of the LMA/YSZ series found that LMA and YSZ coatings are chemically compatible at high temperatures, and the LMA flake grains appearing in the recrystallizing process of the LMA material make the composite coating better sintered resistance and can reduce the density, hardness, and residual stress to 1372 °C has a cycle life of up to 11,749 cycles. Researchers used atmospheric plasma spraying to deposit a new coating with Er_2SiO_5 as the inner layer and LMA material as the top layer on a C/SiC composite. The coating improved high-temperature oxidation resistance but was prone to liquid sintering and bubble formation between the matrix and coating, leading to failure. The LMA/ $\text{Yb}_3\text{Al}_5\text{O}_{12}$ ceramic composite composed of magnetite and garnet structure showed little improvement in LMA material performance. Its thermal conductivity and thermal expansion coefficient at 1200 °C were 3.9 W/(m K) and $8.41 \times 10^{-6} \text{ K}^{-1}$, respectively.

4.3 Other Rare Earth Hexaluminate TBCs Materials

In order to further improve the performance of LMA, the modification of LMA materials with ion doping was studied. The La, Al, and Mg sites of LMA materials were replaced or co-doped. At present, the doped ions of La site mainly include Sr^{2+} , Nd^{3+} , Sm^{3+} , Gd^{3+} , Dy^{3+} , and Yb^{3+} . The doped ions of Al site include Ti^{2+} and Sc^{3+} ions, while the Mg site doping is rarely reported. The incorporation of metal cations can cause point defects and high-density grain boundaries in the crystal structure, which to some extent enhances phonon scattering and thus reduces the thermal conductivity of the material. Sr^{2+} , Zn^{2+} , and Ti^{4+} codoped with LMA material can obtain a lower thermal conductivity of 1.16 W/(m K) at 800 °C. Lu et al. [62] optimized the thermophysical properties of LMA materials by simultaneously replacing La3t and Al ions with Nd3t and Sc3t ions. The results showed that co-substitution had a significant effect on improving the thermal expansion coefficient and reducing the thermal conductivity, which gradually decreased with the increase of ion doping concentration, the lowest thermal conductivity could reach 2.04 W/(m K) at 1000 °C, and the thermal expansion coefficient can reach up to $8.53 \times 10^{-6} \text{ K}^{-1}$. At the same time, the compound doping of Nd^{3+} and Sc^{3+} can also improve the mechanical properties of the material and reduce the conductivity of the material. Li et al. [63] believed that the difference in the negativity between La^{3+} and O^{2-} ions had a negative impact on the increase of the thermal expansion coefficient of the material, so Sm^{3+} and Gd^{3+} ions were selected to partially replace La^{3+} ions to study its thermal properties, and a thermal expansion coefficient of $10.84 \times 10^{-6} \text{ K}^{-1}$ and 1.6 W/(m K) was obtained at 950 °C. The thermal conductivity of and the thermal conductivity coefficient of Dy^{3+} ion doped LMA material at 1200 °C is between 2.52 and 2.89 W/(m K). Wang et al. [64] revealed that the root cause of poor water resistance of LMA materials was the easy position migration of Mg^{2+} ions in the wet environment and proposed that Mg^{2+} ions in the crystal structure of LMA should be completely replaced by

Zn^{2+} ions to improve its delamination resistance, analyzed the root cause of improved delamination resistance, and reduced thermal conductivity of $\text{LaZnAl}_{11}\text{O}_{19}$ materials in depth.

Rare earth titanium-aluminum oxide ($\text{LnTi}_2\text{Al}_9\text{O}_{19}$) is a potential thermal barrier coating (TBC) material with excellent phase stability and ideal thermophysical properties from room temperature to 1600 °C. However, its thermal cycling performance is poor, and its fracture toughness is low. Researchers prepared $\text{LaTi} = \text{Al}_9\text{O}_{19}$ (LTA)/yttrium oxide-stabilized zirconia (YSZ) bilayer TBCs and evaluated their thermal cycle life at a coating surface temperature of 1300 ± 50 °C. Unlike conventional plasma sprayed TBCs, the LTA layer ruptured in the central part of the TBC after approximately 3000 cycles (equivalent to 500 h at 1300 ± 50 °C). Failure was due to decomposition and sintering of LTA exposed to high-temperature gas flame. After another 1000 cycles, the YSZ layer also broke along its interface with the bond layer.

5 Other TBCs Materials

In addition to YSZ, rare earth zirconate, rare earth cerate, and rare earth hexaluminate, other materials with low thermal conductivity are being explored. Each of these materials has advantages and disadvantages. Considering the factors such as thermal expansion coefficient, thermal conductivity, and chemical compatibility of these materials, only a small part of the materials have the potential to be used as a new thermal barrier ceramic layer system.

5.1 Titanate

In recent years, $\text{BaLn}_2\text{Ti}_3\text{O}_{10}$ ($\text{Ln} = \text{La}, \text{Sm}, \text{Nd}$) ceramic materials have also attracted attention, which are potential thermal barrier coating materials due to their lower thermal conductivity, comparable thermal expansion coefficient to YSZ, and good high-temperature phase stability. However, due to the relatively large number of elements in these materials, technological issues such as vapor pressure matching in the spraying process need to be further explored.

$\text{BaLn}_2\text{Ti}_3\text{O}_{10}$ ($\text{Ln}: \text{Sm}, \text{Nd}, \text{Pr}, \text{and La}$) can be synthesized by high-temperature solid-phase reaction and sol-gel methods. Its crystal structure is a layered perovskite with BaO layers inserted into the perovskite block every third layer along the [001] direction. This structure reduces thermal conductivity due to weak bonding between planes containing rigid polyhedra. Lamellar perovskites also show good sintering resistance up to 1773 K and lower thermal conductivity than YSZ. Further studies using plasma spraying (PS) or electron beam physical vapor deposition (EB-PVD) are needed to prepare BLT coatings. Researchers [56] have studied the thermophysical and high-temperature properties of $\text{BaLn}_2\text{Ti}_3\text{O}_{10}$ coatings as a potential TBC material. Guo et al. synthesized $\text{BaLn}_2\text{Ti}_3\text{O}_{10}$ (BLT) by sintering BaCO_3 , TiO_2 , and La_2O_3

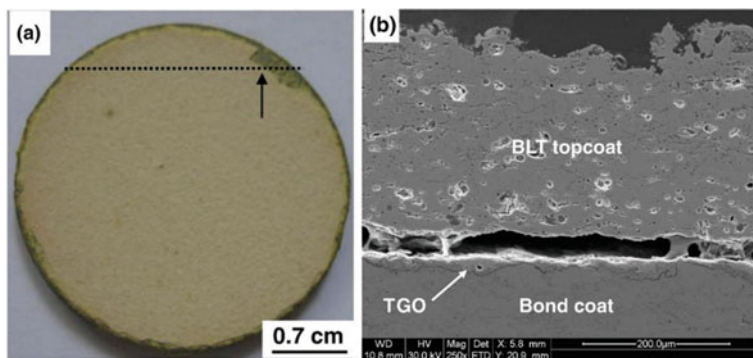


Fig. 13 Photograph (a) and SEM micrograph of cross-section (b) of BLT coating after 1195 thermal cycles. The dashed line and arrow direction of a show the cutting direction and analysis section of the coating [56]

at 1500 °C for 48 h. After sintering at 1500 °C for 110 h, BLT remained phase stable from room temperature to 1400 °C with no decomposition. Its coefficients of thermal expansion (CTEs) are comparable to 7YSZ. BLT coatings prepared by atmospheric pressure plasma spraying have a segmented crack structure and 13% porosity. The micro-hardness is 3.9–4.5 GPa, and thermal conductivity at 1200 °C is about 0.7 W/mK, reduced by about 30% compared to 7YSZ TBCs. Thermal cycling tests show a life exceeding 1100 cycles at 1100 °C. Coating failure occurs due to cracking of the thermal growth oxide (TGO) layer from severe oxidation of the bond layer (Fig. 13).

5.2 Perovskite Structure

The structural atomic composition of perovskite is ABO_3 , and the typical component is $CaTiO_3$. The crystal structure of perovskite is composed of octahedrons with common vertices, which can accommodate various solid ions including large atoms. The most common A-site elements are +2 valent metal ions (Ca^{2+} , Sr^{2+} , Ba^{2+} , Zn^{2+} , Fe^{2+} , Co^{2+} , Ni^{2+} , etc.). The most common B-site elements are +4 valent metal ions (Ti^{4+} , Zr^{4+} , Hf^{4+} , Ru^{4+} , Ce^{4+} , Mo^{4+} , Th^{4+} , U^{4+} , etc.). Most perovskites are stable at high temperature, so they can be used as TBC materials. Alkaline earth zirconate is the most common TBC material in perovskite. $BaZrO_3$ is one of the earliest applications on TBC. Although $BaZrO_3$ has a melting point of up to 2600 °C, its poor thermochemical stability results in poor thermal cycling performance at 1200 °C. In contrast, $SrZrO_3$ has excellent thermal cycling performance when the coating surface temperature exceeds 1250 °C, either as a single layer or as a double ceramic layer deposited on the YSZ surface. The stability of $SrZrO_3$ phase is poor, and it will change from orthogonal to tetragonal phase at 730 °C, which affects the performance of the coating. However, doping Gd and Yb can effectively inhibit this phase transition

and improve the thermal–physical properties of SrZrO₃ coating under extreme high-temperature conditions. As a perovskite-type alkaline earth zirconate, CaZrO₃ has been applied to TBC relatively late. Although its melting point is lower than YSZ, its low thermal conductivity (2 W/m K) makes it a promising new perovskite-type TBC material.

In addition to the high melting point of perovskite, another characteristic is that the B-site atoms are interchangeable, allowing the material's properties to be regulated according to the type of B-site atom. For example, Ba(Mg_{1/3}Ta_{2/3})O₃ has disordered cubic system and ordered tripartite system structure, which is more conducive to the formation of tripartite system structure, especially when the synthesis temperature rises to 1650 °C. The disordered cubic structure of Ba(Mg_{1/3}Ta_{2/3})O₃ coating prepared by APS often exists, and the structure of Ba(Mg_{1/3}Ta_{2/3})O₃ coating is characterized by high temperature (>1250 °C) gradually transformed into an orderly structure during heat treatment. Thermal expansion studies have shown that although this order–disorder transition has some effect on the use of materials, it is not disastrous for the structure of materials. The same B-site arrangement effect also appears in La(Al_{1/4}Mg_{1/2}Ta_{1/4})O₃ material, but this does not affect its use as TBC material. A large number of longitudinal crack networks exist in the coating deposited by APS technology, which is beneficial to reduce the thermal conductivity of the coating and increase the strain tolerance. The microstructure of La(Al_{1/4}Mg_{1/2}Ta_{1/4})O₃ coating applied in the double ceramic layer is shown in Fig. 15. Other properties of this kind of perovskite material are excellent, but the fracture toughness is not as good as YSZ. Due to the high saturated vapor pressure of the oxides in the components, these non-zirconia-based perovskite materials are volatile in the spraying process. The chemical composition of the deposited coating deviates from the standard stoichiometric ratio, which brings serious impact on the performance of the coating. The research shows that by adjusting the spraying parameters to reduce the residence time of the powder particles in the flame, the spraying can be reduced to the greatest extent influence of component volatilization on coating properties during coating. Interestingly, for BaLa₂Ti₃O₁₀, there is no volatilization during the spray process, and no impurity phase deviating from the standard stoichiometric ratio is present in the prepared coating. In addition, because the layered perovskite contains many rigid polyhedrons, the bonding strength between the polyhedrons is weak, which helps to reduce the thermal conductivity, plus the cracking caused by the APS process. The thermal cycling performance of BaLa₂Ti₃O₁₀ coating at 1200 °C is better than YSZ coating due to the effect of the grain. However, due to the low melting point of the material, whether the material can be widely used as TBC at 1200 °C remains to be further investigated.

5.3 Rare Earth Niobate

Rare earth niobate (M₃NbO₇) has two crystal structures: pyrochlore for M = La–Gd and defect fluorite for M = Dy, Lu, Y. The disordered distribution of oxygen vacancies

and large chemical heterogeneity in these structures result in low thermal conductivity with low correlation to temperature. At 25–1000 °C, thermal conductivity is only 1.18–1.26 W/(m K). Research on rare earth niobate TBCs includes introducing rare earth cations to improve mechanical and thermal properties and studying non-standard stoichiometric rare earth niobate by changing elemental composition. Zhu et al. [65] prepared $(\text{Dy}_{0.2}\text{Ho}_{0.2}\text{Er}_{0.2}\text{Y}_{0.2}\text{Yb}_{0.2})_3\text{NbO}_7$ high-entropy rare earth niobate by solid-phase reaction and compared it to single rare earth niobate. The high-entropy rare earth niobate has uniformly distributed rare earth elements forming a single-phase solid solution with increased configuration entropy, resulting in higher Vickers hardness (9.51 HV), fracture toughness ($2.13 \text{ MPa m}^{1/2}$), and thermal expansion coefficient ($10.2 \times 10^{-6} \text{ K}^{-1}$). Due to cation disorder and thermodynamic high-entropy effect, its thermal conductivity is only 0.724 W/(m K), far lower than single rare earth niobate.

In terms of elemental composition, studies on thermal barrier coatings of non-standard stoichiometry are more extensive than those of gadolinium zirconate, while there are few studies on rare earth niobate in this area. Huang et al. [66] analyzed the structure and performance of the coating with non-standard stoichiometric ratio $\text{Y}_{1-x}\text{Nb}_x\text{O}_{1.5+x}$ and found that when the amount ratio of Y/Nb material changes around 3:1, the cationic conductivity of the coating will increase anomalously. In addition, the elastic modulus of the coating will increase with the increase of Nb content. However, due to the inefficient effect of grain size and porosity changes, the Vickers hardness and fracture toughness did not change significantly, and Y_3NbO_7 was found to have the lowest thermal conductivity, the best mechanical properties, and the slowest sintering rate.

Niobate has a ferroelastic toughening mechanism similar to YSZ, with high fracture toughness, and the volume expansion caused by ferroelastic phase transition is basically negligible; that is, it has good high-temperature phase stability. However, the niobate crystal structure lacks intrinsic oxygen vacancies, and the thermal conductivity is higher than other new thermal barrier coating materials, so the performance needs to be further improved.

5.4 Rare Earth Tantalate

Relevant studies show that $\text{ZrO}_2\text{--Y}_2\text{O}_3\text{--Ta}_2\text{O}_5$ terpolymer system has special corrosion resistance (1500 °C), high fracture toughness (equivalent to YSZ fracture toughness), low thermal conductivity, and other advantages, so it has attracted much attention. However, previous studies mainly focused on ZrO_2 rich areas, as shown in Fig. 16, and ZrO_2 material has some bottleneck problems that are difficult to solve at high temperature, so it is a research hot spot to find low thermal conductivity materials from $\text{ZrO}_2\text{--Y}_2\text{O}_3\text{--Ta}_2\text{O}_5$ terpolymer system. Clarke et al. [67] predicted the thermal conductivity of materials in the ternary system of $\text{ZrO}_2\text{--Y}_2\text{O}_3\text{--Ta}_2\text{O}_5$ by using molecular dynamics method. Low thermal conductivity was mainly concentrated in the solid solution region of ZrO_2 and YTao_4 . Figure 16 shows the thermal

conductivity distribution of ZrO_2 - Y_2O_3 - Ta_2O_5 ternary system at 100 and 1000 °C. Thermal conductivity is as low as 1.5 W/(m K) at 1000 °C, which is about 40% lower than YSZ. When the temperature exceeds 1426 ± 7 °C, $YTaO_4$ ceramic will undergo a ferroelastic transition from monoclinic phase to tequartet phase ($M \rightarrow T$), and the volume change is small before and after the phase transition process, thus avoiding martensitic phase transition similar to YSZ, which overcomes the defect of coating failure caused by volume change of YSZ. Therefore, $YTaO_4$ ceramic was considered as a potential ceramic layer material by Clarke et al. (Fig. 14).

In addition, Clarke et al. demonstrated that $YTaO_4$ ceramic had iron-bullet phase transition phenomenon by using the method of first-principles calculation combined with experiment, and ZrO_2 could effectively reduce the iron-bullet phase transition temperature of $YTaO_4$ ceramic. In Fig. 16, the “domain” structure can be clearly observed. SEM results show that twin structures (vertical domain structures within a grain) appear on the grain surface, and the vertical intersections are amplified in the high-resolution transmission electron microscopy images, clearly demonstrating the existence of twin structures (Fig. 15).

Researchers successfully prepared $RETaO_4$ (RE-Nd, Eu, Gd, Dy, Er, Yb, and Lu) ceramics by solid-phase reaction method and systematically studied the thermal and physical properties, as shown in Fig. 17. The thermal conductivity of $RETaO_4$ ceramic is 1.38–1.94 W/(m K) at 800 °C, while that of 8YSZ ceramic is 2.47 W/(m K) at 800 °C, which is reduced by 21–45%. Moreover, this ceramic system has a high coefficient of thermal expansion, which is about $(10\text{--}11) \times 10^{-6} \text{ K}^{-1}$. Some people further reduced the thermal conductivity of $RETaO_4$ by doping, alloying, and other methods and obtained good results. The stability of the crystal structure

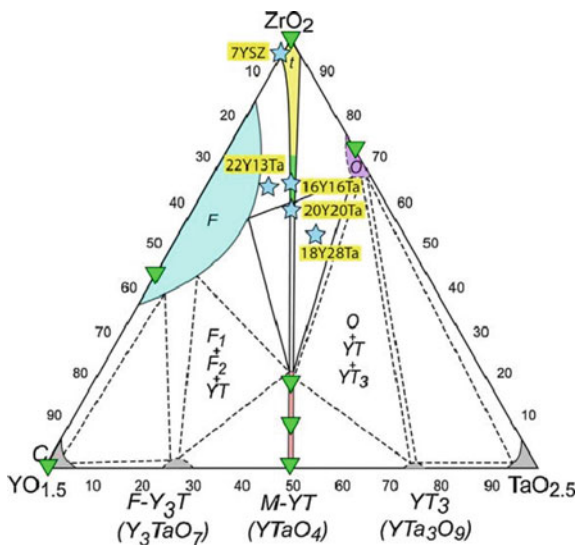


Fig. 14 Isothermal section of the ZrO_2 - Y_2O_3 - Ta_2O_5 phase diagram at 1500 °C [68]

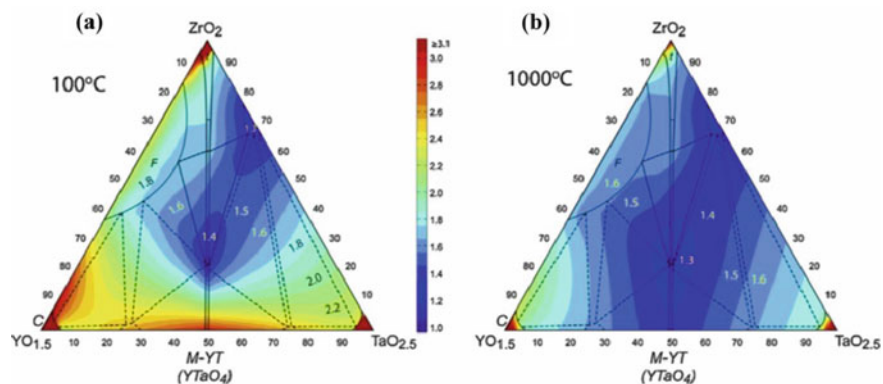


Fig. 15 Thermal conductivity simulation diagram of different components in ZrO_2 - Y_2O_3 - Ta_2O_5 ternary system, **a** 100 °C and **b** 1000 °C [68]

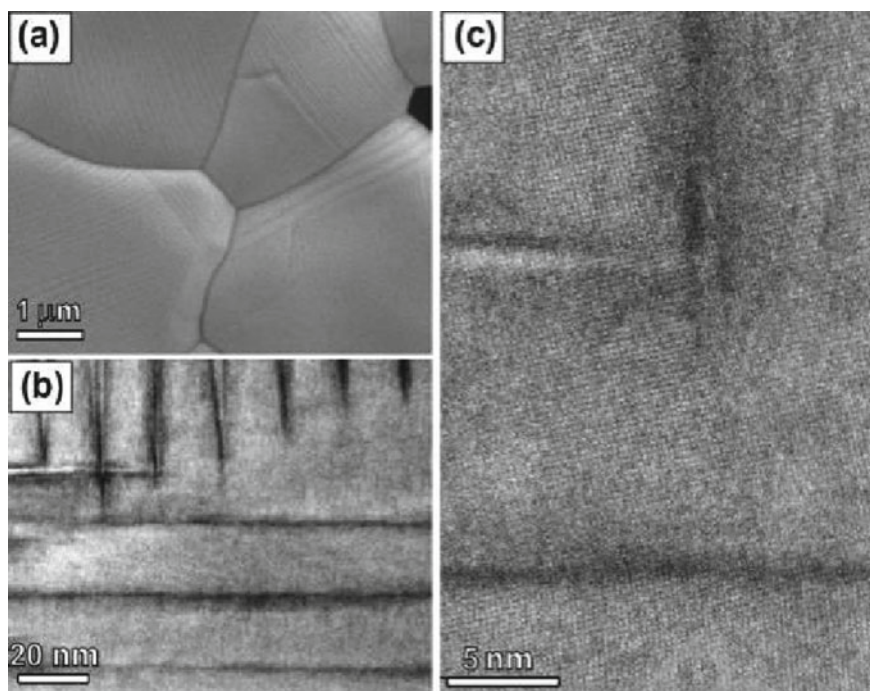


Fig. 16 **a** The SEM of $YTaO_4$ ceramic, **b** the TEM of domain structure for $YTaO_4$ ceramic, and **c** the HRTEM of $YTaO_4$ ceramic [68]

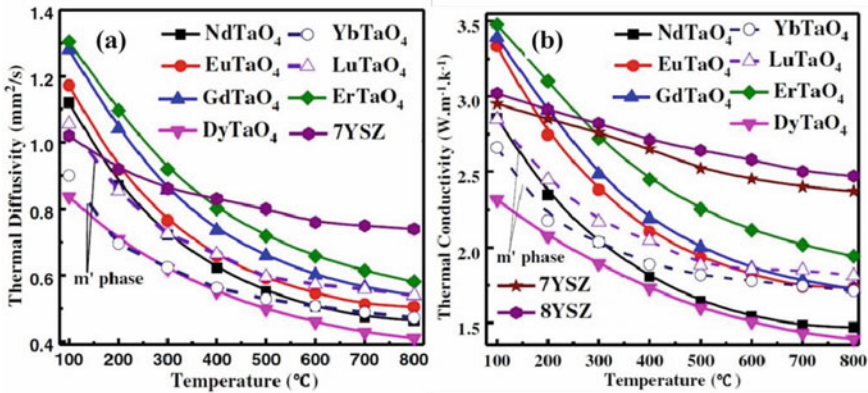


Fig. 17 a Thermal diffusion coefficient and b thermal conductivity of RETaO_4 ceramic [69]

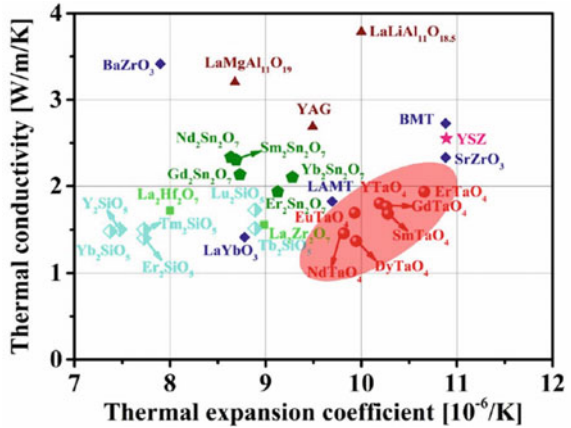
of the system depends on the degree of distortion of Ta–O tetrahedron. There is a certain relationship between Young’s modulus and low Windebye temperature. The reason for the improvement of thermal conductivity at high temperature is attributed to thermal radiation effect.

Figure 18 shows the comparison of thermal conductivity and thermal expansion coefficient between RETaO_4 ceramic and other potential ceramic layer materials. RETaO_4 has relatively low thermal conductivity (1.38–1.94 W/(m K)) and high thermal expansion coefficient ($10\text{--}11 \times 10 \text{ K}^{-1}$). Compared with YSZ, RETaO_4 ’s high-temperature thermal conductivity is only half that of YSZ, and its service temperature can reach 1600 °C, which has obvious advantages. In addition, it is found that RETaO_4 has iron domain structure similar to YSZ, excellent thermal and physical properties and mechanical properties, which further proves that RETaO_4 is a ceramic layer material with great potential. However, at present, there are few researches on the binding mechanism and thermo physical property matching theory of RETaO_4 ceramic and bond layer material, and there is a lack of necessary systematic theoretical analysis and experimental verification.

6 Trend of TBCs Development

As engine technology advances and thrust–weight ratio increases, the working environment of hot-end engine components becomes more severe. High-temperature oxidation, wear, and corrosion can cause irreversible damage to blades. Thermal barrier coatings (TBCs) are necessary to protect their normal operation. Common TBC materials include rare earth doped zirconia, rare earth zirconate, rare earth cerate, rare earth tantalite, and rare earth hexaluminat. Here provides a brief outlook on future TBC materials.

Fig. 18 Schematic diagram of thermal conductivity and thermal expansion of $RETaO_4$ and potential ceramic layer [69]



- (1) To develop nano-thermal barrier coating material preparation technology. Nanoparticles exhibit a series of properties that make nanomaterials a research hot spot. It is an important development direction of thermal barrier coating to introduce nanostructure into thermal barrier coating, which is the advantage of nano-thermal barrier coating. Considering the urgent need of high-performance thermal barrier coating technology for advanced gas turbine engines, the preparation of nano-thermal barrier coating materials and the scientific problems in high-temperature failure were focused to provide theoretical basis for the development of high-performance thermal barrier coating materials, so as to promote the further development of aero-engines and gas turbines.
- (2) To develop related high-entropy rare earth ceramic materials based on potential thermal barrier coating materials and further improve the performance of materials through the unique effects of high-entropy materials. In view of the uncertainty of high-entropy material components, the related concepts of material genetic engineering can be appropriately introduced, and the combination of high-entropy rare earth elements with lower theoretical thermal conductivity better match between CTEs and alloy matrix, and better mechanical properties can be screened through theoretical calculation. Of course, the work on high entropy cannot be limited to rare earth oxides with five components and equimolar components. The research on high-entropy rare earth oxides can be extended to rare earth oxides with more complex components, including medium entropy and non-equimolar components, in order to obtain better coating performance.
- (3) To develop self-healing thermal barrier coating materials. As an important technology, self-healing technology has important applications in the field of corrosion resistance. In terms of thermal barrier coating, self-healing materials can be developed to repair the cracks and voids of the coating, which can effectively reduce the penetration path of oxygen and prevent the formation of TGO, thereby improving the thermal cycling performance of the coating and improving the

thermal shock life of the coating system. At the same time, the self-healing material prevents the penetration of molten corrosion into the coating while repairing cracks and voids. In addition, the closed pores reduce the oxygen diffusivity, further slowing the erosion of the coating system by external impurities, and prolonging the service life of the coating. The time control required for self-healing materials to generate repair oxides is a difficulty in the development of self-healing coatings. The oxide generated under too little oxidation time cannot completely repair the cracks appearing in the coating, and the cracks will still expand in the subsequent high-temperature environment, which also limits the development of self-healing materials.

References

1. Yang, J., Shahid, M., Wan, C., Jing, F., Pan, W.: Anisotropy in elasticity, sound velocities and minimum thermal conductivity of zirconia from first-principles calculations. *J. Eur. Ceram. Soc.* **37**(2), 689–695 (2017)
2. Khattab, E.-S.R., Abd El Rehim, S.S., Hassan, W.M., El-Shazly, T.S.: Band Structure Engineering and Optical Properties of Pristine and Doped Monoclinic Zirconia (m-ZrO₂): density functional theory theoretical prospective. *ACS Omega* **6**(44), 30061–30068 (2021)
3. Lombardo, S., Nelson, C., Chae, K., et al.: Atomic-scale imaging of polarization switching in an (anti-) ferroelectric memory material: Zirconia (ZrO₂). In: 2020 IEEE Symposium on VLSI Technology, pp. 1–2. IEEE (2020)
4. Jose, J., Vigneshwaran, J., Baby, A., Viswanathan, R., Jose, S.P., Sreeja, P.: Dimensionally engineered ternary nanocomposite of reduced graphene oxide/multiwalled carbon nanotubes/zirconium oxide for supercapacitors. *J. Alloy. Compd.* **896**, 163067 (2022)
5. Selvi, S., Nataraj, N., Chen, T.-W., et al.: In-situ formation of 2H phase MoS₂/cerium-zirconium oxide nanohybrid for potential electrochemical detection of an anticancer drug flutamide. *Mater Today Chem* **23**, 100749 (2022)
6. Padture, N.P.: Advanced structural ceramics in aerospace propulsion. *Nat. Mater.* **15**(8), 804–809 (2016)
7. Pan, W., Phillpot, S.R., Wan, C., Chernatynskiy, A., Qu, Z.: Low thermal conductivity oxides. *MRS Bull.* **37**(10), 917–922 (2012)
8. Raghavan, S., Wang, H., Porter, W., Dinwiddie, R., Mayo, M.: Thermal properties of zirconia co-doped with trivalent and pentavalent oxides. *Acta Mater. Mater.* **49**(1), 169–179 (2001)
9. Shen, Z., Liu, Z., Mu, R., He, L., Liu, G.: Y–Er–ZrO₂ thermal barrier coatings by EB-PVD: thermal conductivity, thermal shock life and failure mechanism. *Appl. Surf. Sci. Adv.* (2021)
10. Wei, X., Hou, G., An, Y., Yang, P., Chen, J.: Effect of doping CeO₂ and Sc₂O₃ on structure, thermal properties and sintering resistance of YSZ. *Ceram. Int.* **47**(5) (2020)
11. Khodaii, J., Barzandeh, F., Rezaei, M., Hamed, A., Ahmed, A.D.S.: Influence of grinding parameters on phase transformation, surface roughness, and grinding cost of bioceramic partially stabilized zirconia (PSZ) using diamond grinding wheel. *Int. J. Adv. Manuf. Technol.* **105**(11) (2019)
12. Fan, W., Wang, Z., Bai, Y., et al.: Improved properties of scandia and yttria co-doped zirconia as a potential thermal barrier material for high temperature applications. *J. Eur. Ceram. Soc.* **38**(13), 4502–4511 (2018)
13. Zhao, P., Zheng, H., Li, G., et al.: CMAS corrosion resistant of La³⁺-Yb³⁺-Ce⁴⁺ co-doped ZrO₂ based TBCs: experimental and theoretical research. *Ceram. Int.* **49**(11), 19402–19411 (2023)

14. Rebollo, N.R., Fabrichnaya, O., Levi, C.G.: Phase stability of Y+ Gd co-doped zirconia. *Int. J. Mater. Res.* **94**(3), 163–170 (2022)
15. Liu, Q., Huang, S., He, A.: Composite ceramics thermal barrier coatings of yttria stabilized zirconia for aero-engines. *J. Mater. Sci. Technol.* **35**(12), 2814–2823 (2019)
16. Feng, Y., Dong, T.-s., Li, G.-l., et al.: The roles of stress in the thermal shock failure of YSZ TBCs before and after laser remelting. *J. Alloys Compd.* **828**, 154417 (2020)
17. Lavasani, H.Q., Valefi, Z., Ehsani, N., Masoule, S.T.: Studying the effect of spraying parameters on the sintering of YSZ TBC using APS method. *Surf. Coat. Technol.* **360**, 238–246 (2019)
18. Zhang, H., Liu, Z., Yang, X., Xie, H.: Interface failure behavior of YSZ thermal barrier coatings during thermal shock. *J. Alloy. Compd.* **779**, 686–697 (2019)
19. Jung, S.-H., Lu, Z., Jung, Y.-G., et al.: Thermal durability and fracture behavior of layered Yb-Gd-Y-based thermal barrier coatings in thermal cyclic exposure. *Surf. Coat. Technol.* **323**, 39–48 (2017)
20. Liu, H., Li, S., Li, Q., Li, Y.: Investigation on the phase stability, sintering and thermal conductivity of $\text{Sc}_2\text{O}_3\text{-Y}_2\text{O}_3\text{-ZrO}_2$ for thermal barrier coating application. *Mater. Des.* **31**(6), 2972–2977 (2010)
21. Fan, W., Bai, Y., Wang, Y., et al.: Microstructural design and thermal cycling performance of a novel layer-gradient nanostructured $\text{Sc}_2\text{O}_3\text{-Y}_2\text{O}_3$ co-stabilized ZrO_2 thermal barrier coating. *J. Alloy. Compd.* **829**, 154525 (2020)
22. Wei, Z.-Y., Meng, G.-H., Chen, L., et al.: Progress in ceramic materials and structure design toward advanced thermal barrier coatings. *J. Adv. Ceram.* **11**(7), 985–1068 (2022)
23. Vardelle, A., Moreau, C., Akedo, J., et al.: The 2016 thermal spray roadmap. *J. Therm. Spray Technol.* **25**, 1376–1440 (2016)
24. Goto, T.: Thermal barrier coatings deposited by laser CVD. *Surf. Coat. Technol.* **198**(1–3), 367–371 (2005)
25. Kiilakoski, J., Puranen, J., Heinonen, E., Koivuluoto, H., Vuoristo, P.: Characterization of powder-precursor HVOF-sprayed $\text{Al}_2\text{O}_3\text{-YSZ/ZrO}_2$ coatings. *J. Therm. Spray Technol.* **28**, 98–107 (2019)
26. Lima, R.S., Porous, A.P.S.: YSZ TBC manufactured at high powder feed rate (100 g/min) and deposition efficiency (70%): microstructure, bond strength and thermal gradients. *J. Therm. Spray Technol.* **31**(3), 396–414 (2022)
27. Mauer, G., Jarligo, M.O., Rezanka, S., Hospach, A., VaßEn, R.: Novel opportunities for thermal spray by PS-PVD. *Surf. Coat. Technol.* **268**, 52–57 (2015)
28. Yang, J., Zhao, H., Zhong, X., et al.: Thermal cycling behavior of quasi-columnar YSZ coatings deposited by PS-PVD. *J. Therm. Spray Technol.* (2016)
29. Lashmi, P.G., Ananthapadmanabhan, P.V., Unnikrishnan, G., Aruna, S.T.: Present status and future prospects of plasma sprayed multilayered thermal barrier coating systems. *J. Eur. Ceram. Soc.* **40**(8), 2731–2745 (2020)
30. Schlichting, K.W., Padture, N.P., Jordan, E.H., Gell, M.: Failure modes in plasma-sprayed thermal barrier coatings. *Mater. Sci. Eng. A* **342**(1–2), 120–130 (2003)
31. Soltani, R., Coyle, T.W., Mostaghimi, J.: Creep behavior of plasma-sprayed zirconia thermal barrier coatings. *J. Am. Ceram. Soc.* **90**(9), 2873–2878 (2010)
32. Lima, R.S., Kucuk, A., Berndt, C.C.: Integrity of nanostructured partially stabilized zirconia after plasma spray processing. *Mater. Sci. Eng. A* **313**(1–2), 75–82 (2001)
33. Lima, R.S., Kucuk, A., Berndt, C.C.: Bimodal distribution of mechanical properties on plasma sprayed nanostructured partially stabilized zirconia. *Mater. Sci. Eng. A* **327**(2), 224–232 (2002)
34. Bernier, J.S.: Evolution and characterization of partially stabilized zirconia (7wt% Y_2O_3) thermal barrier coatings deposited by electron beam physical vapor deposition (2002)
35. Zhang, B., Song, W., Wei, L., et al.: Novel thermal barrier coatings repel and resist molten silicate deposits. *Scripta Mater. Mater.* **163**, 71–76 (2019)
36. Gao, L., Guo, H., Wei, L., Li, C., Xu, H.: Microstructure, thermal conductivity and thermal cycling behavior of thermal barrier coatings prepared by plasma spray physical vapor deposition. *Surf. Coat. Technol.*, 424–430 (2015)

37. Li, C., Guo, H., Gao, L., Wei, L., Gong, S., Xu, H.: Microstructures of yttria-stabilized zirconia coatings by plasma spray-physical vapor deposition. *J. Therm. Spray Technol.* **24**, 534–541 (2015)
38. Shan, X., Zou, Z., Gu, L., et al.: Buckling failure in air-plasma sprayed thermal barrier coatings induced by molten silicate attack. *Scripta Mater. Mater.* **113**, 71–74 (2016)
39. Thornton, J., Wood, C., Kimpton, J.A., Sesso, M., Zonneveldt, M., Armstrong, N.: Failure mechanisms of calcium magnesium aluminum silicate affected thermal barrier coatings. *J. Am. Ceram. Soc.* **100**(6), 2679–2689 (2017)
40. Wang, Z., Zhou, G., Jiang, D., Wang, S.: Recent development of $A_2B_2O_7$ system transparent ceramics. *J. Adv. Ceram.* **7**(4), 289–306 (2018)
41. KräMer, S., Yang, J., Levi, C.G.: Infiltration-inhibiting reaction of gadolinium zirconate thermal barrier coatings with CMAS melts. *J. Am. Ceram. Soc.* **91**(2), 576–583 (2010)
42. Wang, C., Huang, W., Wang, Y., et al.: Synthesis of monodispersed $La_2Ce_2O_7$ nanocrystals via hydrothermal method: a study of crystal growth and sintering behavior. *Int. J. Refract Metal Hard Mater.* **31**, 242–246 (2012)
43. Lehmann, H., Pitzer, D., Pracht, G., Vassen, R., Stöver, D.: Thermal conductivity and thermal expansion coefficients of the lanthanum rare-earth-element zirconate system. *J. Am. Ceram. Soc.* **86** (2010)
44. Wan, C.L., Pan, W., Xu, Q., Qin, Y.X., Fang, M.H.: Effect of point defects on the thermal transport properties of $(La_xGd_{1-x})_2Zr_2O_7$: experiment and theoretical model. *Physrevb* **74**(14), 144109 (2006)
45. Wan, C., Wei, Z., Wang, Y., et al.: Glass-like thermal conductivity in ytterbium-doped lanthanum zirconate pyrochlore. *Acta Mater. Mater.* **58**(18), 6166–6172 (2010)
46. Cao, X., Li, J., Zhong, X., et al.: $La_2(Zr_{0.7}Ce_{0.3})_2O_7$ —a new oxide ceramic material with high sintering-resistance. *Mater. Lett.* **62**(17–18), 2667–2669 (2008)
47. Cao, X., Vassen, R., Stöver, D.: Ceramic materials for thermal barrier coatings. *J. Eur. Ceram. Soc.* **24**(1), 1–10 (2004)
48. Taleghani, P.R., Valefi, Z., Ehsani, N.: Synthesis of $La_2(Zr_{0.7}Ce_{0.3})_2O_7$ nanopowder using a simple chemical precipitation method and heat treatment at high temperature. *Int. J. Mater. Res.* **110**(8), 757–764 (2019)
49. Kutty, K., Rajagopalan, S., Mathews, C.K., Varadaraju, U.V.: Thermal expansion behaviour of some rare earth oxide pyrochlores. *Mater. Res. Bull.* **29**(7), 759–766 (1994)
50. Shimamura, K., Arima, T., Idemitsu, K., Inagaki, Y.: Thermophysical properties of rare-earth-stabilized zirconia and zirconate pyrochlores as surrogates for actinide-doped zirconia. *Int. J. Thermophys. Thermophys.* **28**, 1074–1084 (2007)
51. Schelling, P., Phillpot, S., Grimes, R.: Optimum pyrochlore compositions for low thermal conductivity. *Philos. Mag. Lett.* **84**(2), 127–137 (2004)
52. Li, J.Y., Dai, H., Li, Q., Zhong, X.H., Cao, X.Q.: Improvement of fracture toughness lanthanum zirconate. *Mater. Eng.* **2006**(5) (2006)
53. Li, J., Dai, H., Li, Q., Zhong, X., Cao, X.: Improvement of fracture toughness lanthanum zirconate. *Cailiao Gongcheng* **5**, 51–56 (2006)
54. Zhu, Z., Liu, B., Shen, J., Lou, Y., Ji, Y.: $La_2Ce_2O_7$: a promising proton ceramic conductor in hydrogen economy. *J. Alloy. Compd.* **659**, 232–239 (2016)
55. Praveen, K., Sravani, N., Alroy, R.J., Shanmugavelayutham, G., Sivakumar, G.: Hot corrosion behaviour of atmospheric and solution precursor plasma sprayed $(La_{0.9}Gd_{0.1})_2Ce_2O_7$ coatings in sulfate and vanadate environments. *J. Eur. Ceram. Soc.* **39**(14), 4233–4244 (2019)
56. Guo, H., Gong, S., Xu, H.: Evaluation of hot-fatigue behaviors of EB-PVD gradient thermal barrier coatings. *Mater. Sci. Eng. A* **325**(1–2), 261–269 (2002)
57. Heveling, J.: La-doped alumina, lanthanum aluminate, lanthanum hexaaluminate, and related compounds: a review covering synthesis, structure, and practical importance. *Ind. Eng. Chem. Res.* **62**(6), 2353–2386 (2023)
58. Pan, W., Xu, Q., Qi, L., et al.: Novel low thermal conductivity ceramic materials for thermal barrier coatings. In: *China International Conference on High-Performance Ceramics* (2005)

59. Machida, M., Kawasaki, H., Eguchi, K., Arai, H.: Surface areas and catalytic activities of Mn-substituted hexaaluminates with various cation compositions in the mirror plane. *Chem. Lett.* **17**(9), 1461–1464 (1988)
60. Sun, J., Hui, Y., Jiang, J., Deng, L., Cao, X.: Crystallization mechanism of plasma-sprayed LaMgAl₁₁O₁₉ coating. *Appl. Surf. Sci.* **504**, 144509 (2019)
61. Chen, X., Zhao, Y., Fan, X., et al.: Thermal cycling failure of new LaMgAl₁₁O₁₉/YSZ double ceramic top coat thermal barrier coating systems. *Surf. Coat. Technol.* **205**(10), 3293–3300 (2011)
62. Lu, H., Wang, C.-A., Zhang, C.: Low thermal conductivity Sr²⁺, Zn²⁺ and Ti⁴⁺ ions co-doped LaMgAl₁₁O₁₉ for potential thermal barrier coating applications. *Ceram. Int.* **40**(10), 16273–16279 (2014)
63. Li, W., Zhou, X., Lei, Q., Wang, S.: Heat and moisture resistance of divalent metals substituted La-Hexaaluminates prepared by reverse microemulsion. *Ceram. Int.* (2020)
64. Wang, Y.-H., Ouyang, J.-H., Liu, Z.-G.: Influence of dysprosium oxide doping on thermophysical properties of LaMgAl₁₁O₁₉ ceramics. *Mater. Des.* **31**(7), 3353–3357 (2010)
65. Zhu, Y., Wang, X., Wang, A., Wu, G., Wang, J., Zhang, T.: Identification of the chemical state of Fe in barium hexaaluminate using Rietveld refinement and 57Fe Mössbauer spectroscopy. *J. Catal. Catal.* **283**(2), 149–160 (2011)
66. Huang, C., Zhou, X., Ding, C.: Investigation of the thermomechanical properties of a plasma-sprayed nanostructured zirconia coating. *J. Eur. Ceram. Soc.* **23**(9), 1449–1455 (2003)
67. Clarke, D., Levi, C.: Materials design for the next generation thermal barrier coatings. *Annu. Rev. Mater. Res.* *Rev. Mater. Res.* **33**(1), 383–417 (2003)
68. Limarga, A.M., Shian, S., Leckie, R.M., Levi, C.G., Clarke, D.R.: Thermal conductivity of single-and multi-phase compositions in the ZrO₂-Y₂O₃-Ta₂O₅ system. *J. Eur. Ceram. Soc. Ceram. Soc.* **34**(12), 3085–3094 (2014)
69. Wang, J., Chong, X.Y., Zhou, R., Feng, J.: Microstructure and thermal properties of RETaO₄ (RE = Nd, Eu, Gd, Dy, Er, Yb, Lu) as promising thermal barrier coating materials. *Scripta Materialia* **126**(Complete), 24–28 (2017)